

1 Local wind regime induced by giant linear dunes:
2 comparison of ERA5-Land re-analysis with surface
3 measurements

4 Cyril Gadal · Pauline Delorme ·
5 Clément Narteau · Giles F.S. Wiggs ·
6 Matthew Baddock · Joanna M. Nield ·
7 Philippe Claudin

8
9 Received: DD Month YEAR / Accepted: DD Month YEAR

10 **Abstract**

11 Emergence and growth of sand dunes results from the dynamic interaction
12 between topography, wind flow and sediment transport. While feedbacks be-
13 tween these variables are well studied at the scale of a single dune, the average
14 effect of a periodic dune pattern on atmospheric flows remains poorly con-
15 strained due to a lack of data in major sand seas. Here, we compare ~~field-wind~~
16 ~~tower~~ measurements of surface wind data to the predictions of the ERA5-Land
17 climate reanalysis at four locations in Namibia, ~~including within and~~
18 ~~outside~~ the giant-dune field of the Namib sand sea. In the desert plains to the
19 north of the sand sea, observations and predictions agree well. This is also
20 the case in the interdune areas of the sand sea ~~during the day, but not during~~
21 ~~the night, except for the weak winds blowing at night, which exhibit where~~
22 additional components aligned with the giant dune orientation, ~~which are not~~

C. Gadal

Institut de Mécanique des Fluides de Toulouse, Université de Toulouse Paul Sabatier, CNRS,
Toulouse INP-ENSEEIHT, Toulouse, France. E-mail: cyril.gadal@imft.fr

P. Delorme

Energy and Environment Institute, University of Hull, Hull, UK.

C. Narteau

Institut de Physique du Globe de Paris, Université de Paris, CNRS, Paris, France.

G. Wiggs

School of Geography and the Environment, University of Oxford, Oxford, UK.

M. Baddock

Geography and Environment, Loughborough University, Loughborough, UK.

J.M. Nield

School of Geography and Environmental Science, University of Southampton, Southampton,
UK.

P. Claudin

Physique et Mécanique des Milieux Hétérogènes, CNRS, ESPCI Paris, PSL Research Uni-
versity, Université de Paris, Sorbonne Université, Paris, France.

are measured instead of the easterly wind predicted by the ERA5-Land reanalysis. We quantify these similarities and differences and provide a physical understanding of the relevant aerodynamical regimes to relate them. These discrepancies, with wind deviation and attenuation larger than 50° and 60 %, are linked to the daily cycle of the turbulent atmospheric boundary layer over a dune pattern of given wavelength. We conclude by identifying the conditions under which the ERA5-Land reanalysis data can reliably be used to study dune morphodynamics. We also complex topography, and to the associated flow regimes. During the night, the low wind velocities within a shallow boundary layer induces a flow confinement, leading to a strong streamline compression above the giant dunes and thus resulting in large flow deviations. During the day, the flow confinement is reduced by higher wind velocities and deep boundary layers. We finally propose that, in multidirectional wind regimes, deflections of specific winds this mechanism and the resulting wind deflections by giant dunes could explain the occurrence of secondary dune patterns with a different orientation elongating in different orientations compared to the primary structures between which they develop.

Keywords Atmospheric boundary layer · Sand dunes · Flow over hills

41 1 Introduction

42 The description of turbulent flows over complex topography is relevant for a
43 large variety of different environmental systems (Finnigan et al. 2020)(Sherman 1978; Walmsley et al. 1982; Baines 1995;
44 . For example, the flow over hills is of primary interest for wind power, me-
45 teorological and air pollution phenomena (Taylor et al. 1987). The prop-
46 erties of these flows are also key to the understanding of geophysical phe-
47 nomena, including the formation of wind-driven waves on the ocean surface
48 (Sullivan and McWilliams 2010), dissolution bedforms (Claudin et al. 2017)
49 (Claudin et al. 2017; Guérin et al. 2020), or sedimentary ripples and dunes
50 (Charru et al. 2013; Courrech du Pont 2015)(Bagnold 1941; Charru et al. 2013; Courrech du Pont 2015)
51 . Importantly, the troposphere presents a vertical structure, with a lower con-
52 vective boundary layer, of typical kilometer-scale thickness, capped by a stably
53 stratified region (Stull 1988). The largest topographic obstacles, such as moun-
54 tains, can therefore interact with this upper region and lead to internal wave
55 generation or significant wind disturbances, such as lee-side downslope winds
56 (Durran 1990).

57 ~~Focusing on the wind close to the surface, Compared to mountains, aeolian~~
58 ~~sand dunes offer idealized topographies to the study of atmospheric turbulent~~
59 ~~flow over wavy bottoms, due to their smooth shape, free of canopies, resulting~~
60 ~~from their interaction with the wind (Bagnold 1941). Then, past studies have~~
61 ~~highlighted two related topographic feedbacks on the windflow over dunes can~~
62 ~~be commented on separately close to the dune/hill surface.~~ First is the effect
63 on wind speed, with documented flow acceleration on upwind slopes (Weaver
64 and Wiggs 2011) and deceleration on downwind slopes (Baddock et al. 2007),
65 where the speed-up factor is essentially proportional to the obstacle aspect ra-
66 tio (Jackson and Hunt 1975). Importantly, the velocity maximum is typically
67 shifted upwind of the obstacle crest (Jackson and Hunt 1975; Claudin et al. 2013)
68 . This behaviour has been theoretically predicted by means of asymptotic anal-
69 ysis of a neutrally stratified boundary-layer flow over an obstacle of vanishing
70 aspect ratio (Jackson and Hunt 1975; Mason and Sykes 1979; Sykes 1980; Hunt
71 et al. 1988; Belcher and J.C.R. 1998). Experiments in flumes (Zilker et al. 1977;
72 Zilker and Hanratty 1979; Frederick and Hanratty 1988; Poggi et al. 2007; Bris-
73 tow et al. 2022), in wind tunnels (Gong and Ibbetson 1989; Finnigan et al.
74 1990; Gong et al. 1996) and in field conditions ~~at all scales~~ (Taylor and Teu-
75 nissen 1987; Claudin et al. 2013; Fernando et al. 2019; Lü et al. 2021), have
76 also documented this effect. Interestingly, a similar behaviour exists for the
77 pressure perturbation, but with a slight downwind shift for the pressure min-
78 imum (Claudin et al. 2021). The second effect, much less studied, is the flow
79 deflection that occurs when the incident wind direction is not perpendicular to
80 the ridge crest. While predicted to be small (less than 10°) in the linear regime
81 valid for shallow topography (Gadal et al. 2019), significant flow steering has
82 been reported in the field on the downwind side of steep enough obstacles, such
83 as mountain ranges (Kim et al. 2000; Lewis et al. 2008; Fernando et al. 2019)
84 , well-developed sand dunes (Walker et al. 2009; Hesp et al. 2015; Walker et al. 2017; Smith et al. 2017; de Winter et al.
85 (Tsoar and Yaalon 1983; Sweet and Kocurek 1990; Walker and Nickling 2002; Smith et al. 2017)

and in particular coastal foredunes (e.g. Rasmussen (1989), Walker et al. (2006), Walker et al. (2009), Hesp et al. (2015), Walker et al. (2017), de Winter et al. (2020)), mountain ranges (Kim et al. 2000; Lewis et al. 2008; Fernando et al. 2019), and valley topographies (Wiggs et al. 2002; Garvey et al. 2005).

For practical reasons, wind measurement Wind measurements over sand dunes has been mainly performed over small bedforms, typically a few meters high (corresponding to tens of meters long) (e.g. Mulligan (1988), Hesp et al. (1989), Lancaster et al. (1996), Mckenna Neuman et al. (1997), Sauermann et al. (2003), Andreotti et al. (2002), Walker and Nickling (2002), Weaver and Wiggs (2011)). Giant dunes For practical reasons, fewer studies performed similar measurements on giant dunes (Havholm and Kocurek 1988), with kilometer-scale wavelengths and heights of tens of meters, are more difficult to investigate although for several reasons. However, they provide a choice configuration for the study of turbulent flows over a complex topography. First, one expects larger wind disturbances for larger obstacles. Secondly, their large size makes them interact with the vertical structure of the atmosphere (Andreotti et al. 2009). Third, they usually form large patterns in sand seas and thus behave as rather clean periodic perturbations, in contrast with isolated dunes. Finally, because the morphodynamics of aeolian bedforms are strongly dependent on the local wind regime (Livingstone and Warren 2019), one can expect to see the consequences of windflow disturbance by large dunes on neighbouring small dunes (Brookfield 1977; Ewing et al. 2006). A similar effect is observed on the properties of impact ripple patterns due to the presence of dunes (Howard 1977; Hood et al. 2021)(Howard 1977; Hood et al. 2021).

Atmospheric flows have been much studied at the desert-scale with climate reanalyses based on global atmospheric models (Blumberg and Greeley 1996; Livingstone et al. 2010; Ashkenazy et al. 2012; Jolivet et al. 2021; Hu et al. 2021), such as ERA-40, ERA-Interim or ERA-5 (Uppala et al. 2005; Dee et al. 2011; Hersbach et al. 2020). However, the spatial resolution (tens of kilometers) of these reanalyses implies average quantities that do not resolve the smaller scales of interest, which range from individual dunes to small mountains (Livingstone et al. 2010). Recently, the release of ERA5-Land has resolved this limitation by providing up to 70 years of hourly wind predictions at a 9 km spatial resolution (Muñoz-Sabater et al. 2021). However, its validity remains to be studied, especially in remote desert areas where assimilation of measured data is very low.

In this work, we compare local wind speeds and directions measured by meteorological stations at four different locations inside and north of the giant-dune field of the Namib sand sea to the regional predictions of the ERA5-Land climate reanalysis. Where the meteorological stations are surrounded by a relatively flat environment, we show that local measurements and regional predictions agree well. The agreement is also good in the interdune areas of the sand sea, except for some weak winds blowing at night, which exhibit an additional component aligned with the giant dune orientation. These winds are not predicted by the ERA5-Land reanalysis (section 2). Further, we are able to link the magnitude of these differences to the circadian cycle of the

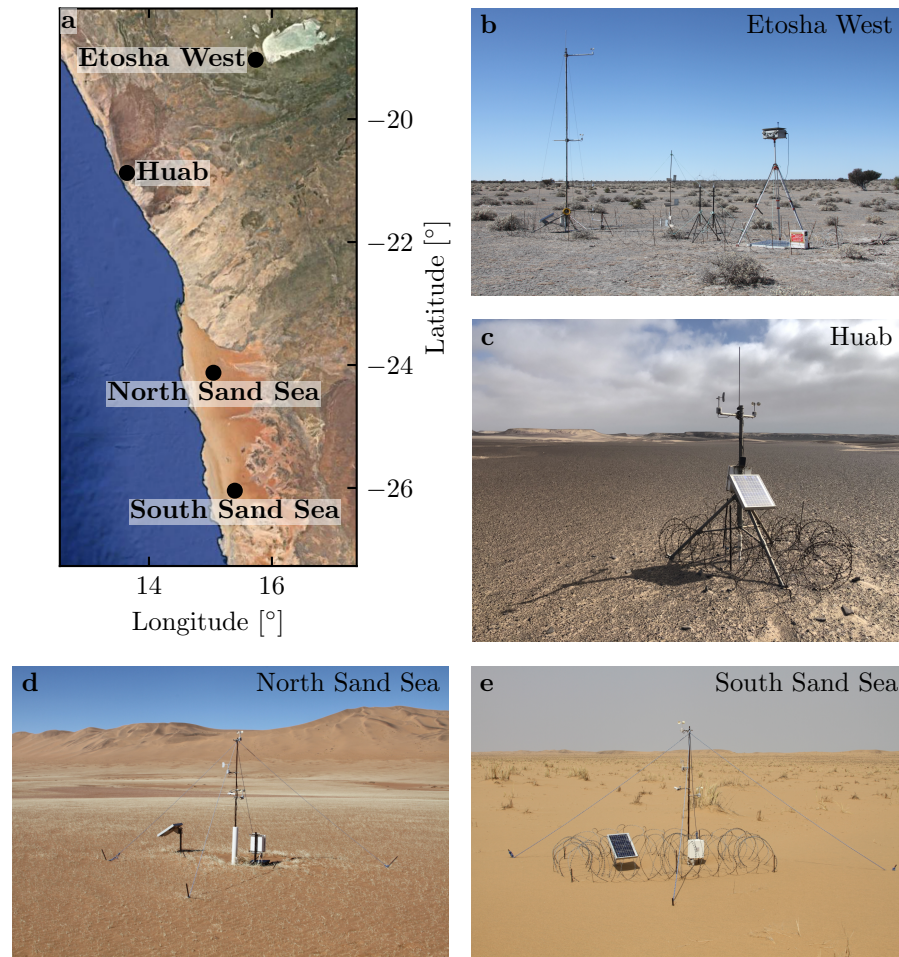


Fig. 1 Wind data used in this study Studied field sites. **a:** Location of the different sites in Namibia. **b–e:** Satellite images Photographs of these different environments (Google-Earth, Maxar Technologies, CNES/Airbus). In each subplot, the left and right wind roses represent the data from the ERA5-Land climate reanalysis and the local wind stations, respectively. Note that the bars show the direction towards which the wind blows. The black dots show the location of local wind meteorological stations.

atmospheric boundary layer (section 3). Finally, we draw implications for the wind disturbances on smaller-scale dunes (section 4), suggesting a possible origin for crossing dunes.

2 Wind regimes across the Namib Sand Sea

We measured the wind regime at four different locations in Namibia, representative of various arid environments across the Namib desert (Fig. 1, [Online](#)

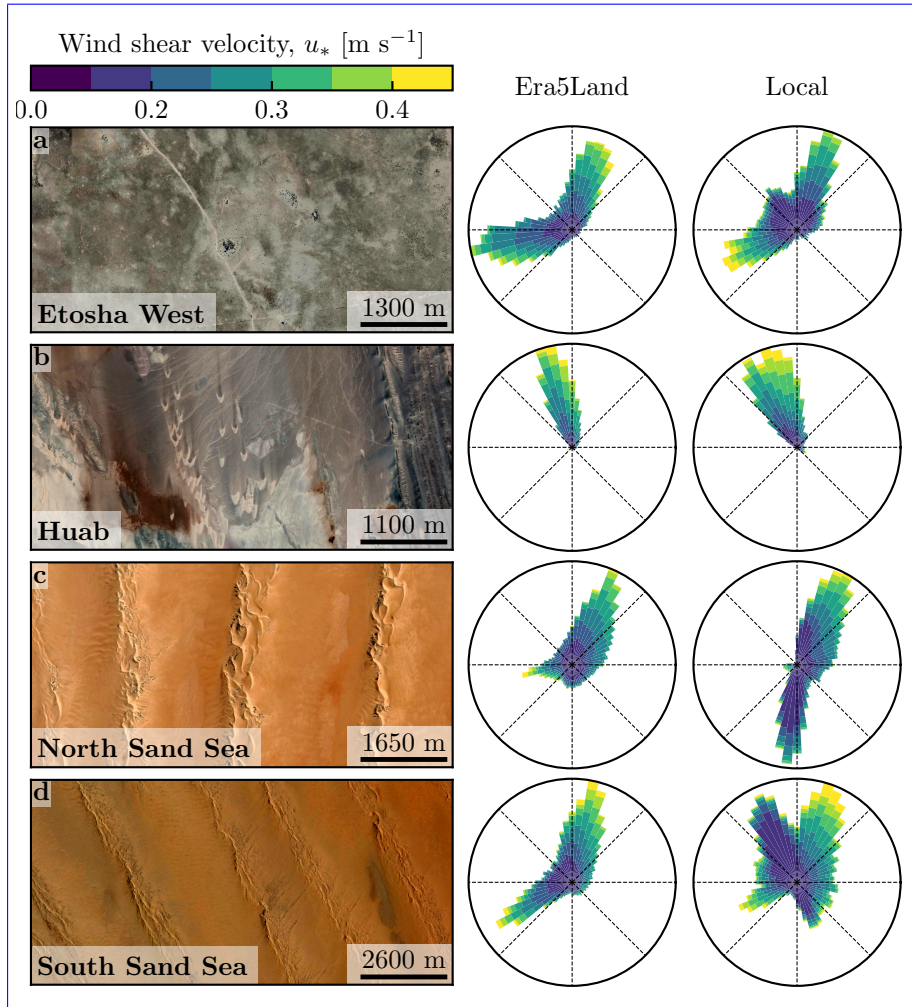


Fig. 2 Wind data used in this study. Satellite images of these different environments (Google-Earth, Maxar Technologies, CNES/Airbus) are shown on the left. The black dots show the location of the wind measurements stations. On the center and on the right, wind roses representing the data from the ERA5-Land climate reanalysis and the local wind stations are respectively shown. Note that the bars show the direction towards which the wind blows.

138 **Resource**—Fig. 42). The Etosha West station was located at the Adamax wa-
 139 terhole to the west of Etosha Pan in northern Namibia, in a sparsely vegetated
 140 area. The Huab station was near the coast on a hyper-arid flat gravel plain
 141 lying north the ephemeral Huab river. Here, barchan dunes up to a few me-
 142 ters in height develop from the sediment blowing out of the river valley (Nield
 143 et al. 2017; Hesp and Hastings 1998). These two stations were both located
 144 in relatively flat environments. In contrast, the North Sand Sea and South

145 Sand Sea stations were located in the interdunes between linear dunes with
146 kilometer-scale wavelengths, hectometer-scale heights and superimposed pat-
147 terns. In this section, we describe and compare winds from local measurements
148 and climate reanalysis predictions.

149 2.1 Wind and elevation data

150 At each meteorological station (Fig. 1), wind speed and direction were sam-
151 pled every 10 minutes using cup anemometers (Vector Instruments A100-LK)
152 and wind vanes (Vector Instruments W200-P) at ~~heights which varied a single~~
153 ~~height, which was~~ between 2 m and 3 m depending on the station. The avail-
154 able period of measurements at each station ranged from 1 to 5 discontinuous
155 years distributed between 2012 and 2020 (Online Resource Fig. S24). We
156 checked that at least one complete seasonal cycle was available for each sta-
157 tion. Regional winds were extracted at the same locations and periods from
158 the ERA5-Land dataset, which is a replay at a smaller spatial resolution of
159 ERA5, the latest climate reanalysis from the ECMWF (Hersbach et al. 2020;
160 Muñoz-Sabater et al. 2021). This dataset provided hourly predictions of the
161 10-m wind velocity and direction at a spatial resolution of $0.1^\circ \times 0.1^\circ$ (≈ 9 km
162 in Namibia).

163 To enable direct comparison, the local wind measurements were averaged
164 into 1-hr bins centered on the temporal scale of the ERA5-Land estimates
165 (Online Resource Fig. S3S2). As the wind velocities of both datasets were pro-
166 vided at different heights, we converted them into shear velocities u_* (Online
167 Resource section 1), characteristic of the turbulent wind profile. Wind roses
168 in Fig. 1(b-e)-2 show the resulting wind data.

169 Dune properties were computed using autocorrelation on the 30-m Digital
170 Elevation Models (DEMs) of the shuttle radar topography mission (Farr et al.
171 2007). For the North and South Sand Sea stations, we obtain, respectively,
172 orientations of 85° and 125° with respect to the North, wavelengths of 2.6 km
173 and 2.3 km and amplitudes (or half-heights) of 45 m and 20 m (Online Resource
174 Fig. S5-S4 for more details). This agrees with direct measurements made on
175 site.

176 2.2 Comparison of local and regional winds

177 The measured and predicted wind regimes are shown in Fig. 42. In the Namib,
178 the regional wind patterns are essentially controlled by the sea breeze, result-
179 ing in strong northward components (sometimes slightly deviated by the large
180 scale topography) present in all regional wind roses (Lancaster 1985). These
181 daytime winds are dominant during the period October-March (Fig. 23f and
182 Online Resource Fig. S64f). During April-September, an additional (and often
183 nocturnal) easterly component can also be recorded, induced by the combina-
184 tion of katabatic winds forming in the mountains, and infrequent ‘berg’ winds,

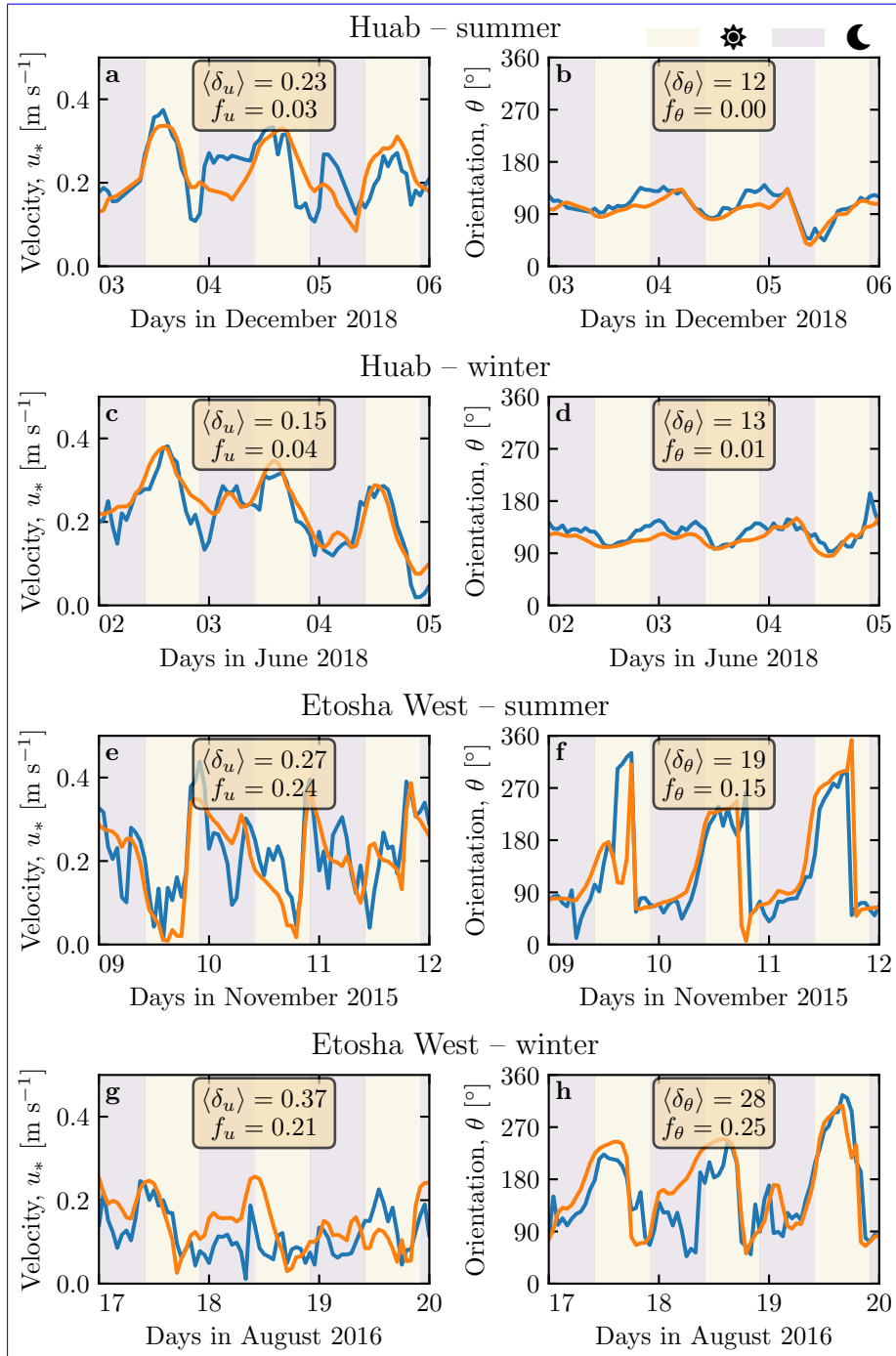


Fig. 3 Temporal comparison between the wind data coming from the ERA5-Land climate reanalysis (orange lines) and from the local measurements (blue lines). Coloured swathes indicate day (between 1000 UTC and 2200 UTC) and night (before 1000 UTC or after 2200 UTC). Numbers indicate the average flow deflection δ_θ and wind modulation δ_u over the given period, as well as the frequency of occurrence of extreme events ($\delta_\theta > 50^\circ$, $|\delta_u| > 0.6$). **a–b:** Etosha West Huab station in summer. **b–c:** Etosha West Huab station in winter. **d–e:** North Sand Sea Etosha West station in summer. **f–g:** North Sand Sea Etosha West station in winter. Time series of the two other stations are shown in [Online Resource Fig. S65](#).

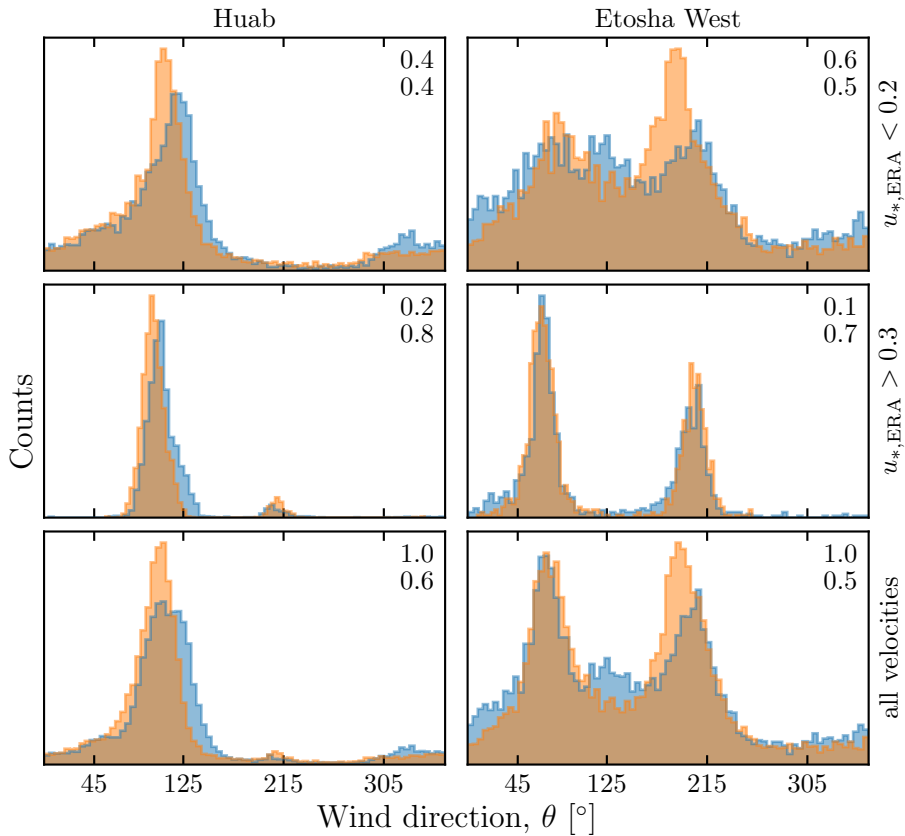


Fig. 4 Distributions of wind direction at the Huab and Etosha West stations for the ERA5-Land climate reanalysis (orange) and the local measurements (blue). In each subplot, both distributions are plotted from the same time steps, selected with constraints on the wind wind velocity (rows) in the ERA5-Land dataset. The numbers at the top centre give the percentage of time steps selected in each sub-range, as well as the percentage of them corresponding to the day (between 1000 UTC and 2200 UTC).

which are responsible for the high wind velocities observed (Lancaster et al. 1984). The frequency of these easterly components decreases from inland to the coast. As a result, bidirectional wind regimes within the Namib Sand Sea and at the west Etosha site (Fig. 4b,d,e2a,c,d) and a unidirectional wind regime on the coast at the outlet of the Huab River (Fig. 4e2b) are observed.

In the case of the Etosha West and Huab stations, the time series of wind speed and direction from the regional predictions quantitatively match those corresponding to the local measurements (Fig. 2a-d) Figs. 3, 4 and Online Resource Figs. S6a-d, S7, S9 Fig. S5). For the North Sand Sea and South Sand Sea stations within the giant dune field, we observe that this agreement is also good, but limited to the October-March time period (Fig. 2e-h and and Online Resource Fig. S6e-h 4a, b, e, f). However, the field-measured wind roses

¹⁹⁷ exhibit additional wind components aligned with the giant dune orientation,
¹⁹⁸ as evidenced on the satellite images (Fig. 42c,d).

¹⁹⁹ More precisely, during the April-September period, the local and regional
²⁰⁰ winds in the interdune match during daytime only, i.e when the southerly/-
²⁰¹ southwesterly sea breeze dominates (Figs. 2e,f and 3, Online Resource Fig. S85c,d,g,h
²⁰² and 6). In the late afternoon and during the night, when the easterly ‘berg’ and
²⁰³ katabatic winds blow, measurements and predictions differ. In this case, the
²⁰⁴ angular wind distribution of the local measurements exhibits two additional
²⁰⁵ modes corresponding to reversing winds aligned with the giant dune orienta-
²⁰⁶ tion (purple frame in Fig. 36, Online Resource Figs. S8 and S10 Fig. S6). This
²⁰⁷ deviation is also associated with a general attenuation of the wind strength
²⁰⁸ (Online Resource Fig. S11S7). Remarkably, all these figures show that these
²⁰⁹ wind reorientation and attenuation processes occur only at low velocities of
²¹⁰ the regional wind, typically for $u_{*,\text{ERA}} \lesssim 0.2 \text{ m s}^{-1}$. For shear velocities larger
²¹¹ than $u_{*,\text{ERA}} \simeq 0.3 \text{ m s}^{-1}$, the wind reorientation is not apparent. Finally, for
²¹² intermediate shear velocities, both situations of wind flow reoriented along the
²¹³ dune crest and not reoriented can be successively observed (Online Resource
²¹⁴ Fig. S10S6). Importantly, these values are not precise thresholds, but indica-
²¹⁵ tive of a crossover between regimes, whose physical interpretation is discussed
²¹⁶ in the next section.

²¹⁷ 3 Influence of wind speed and circadian cycle on the atmospheric ²¹⁸ boundary layer

²¹⁹ The wind deflection induced by linear dunes has previously been related to the
²²⁰ incident angle between wind direction and crest orientation, with a maximum
²²¹ deflection evident for incident angles between 30° and 70° (Walker et al. 2009;
²²² Hesp et al. 2015). In the data analysed here, the most deflected wind at both
²²³ the North and South Sand Sea stations is seen to be where the incident angle
²²⁴ is perpendicular to the giant dunes (Figs. 1 and 3, Online Resource Fig. S82
²²⁵ and 6). It therefore appears that in our case, the incident wind angle is not
²²⁶ the dominant control on maximum wind deflection. Further, and as shown
²²⁷ in Fig. 36, winds of high and low velocities show contrasting behaviour in
²²⁸ characteristics of deflection. This suggests a change in hydrodynamical regime
²²⁹ between the winds. In this section, we discuss the relevant parameters associ-
²³⁰ ated with the dynamical mechanisms that govern the interactions between the
²³¹ atmospheric boundary layer flow and giant dune topographies. This analysis
²³² allows us to provide a physics-based interpretation of our measured wind data.

²³³ 3.1 Flow over a modulated bed

²³⁴ Taking as a reference the turbulent flow over a flat bed, the general framework
²³⁵ of our study is understanding and describing the flow response to a bed mod-
²³⁶ ulation (e.g. a giant dune). Without loss of generality, we can consider in this

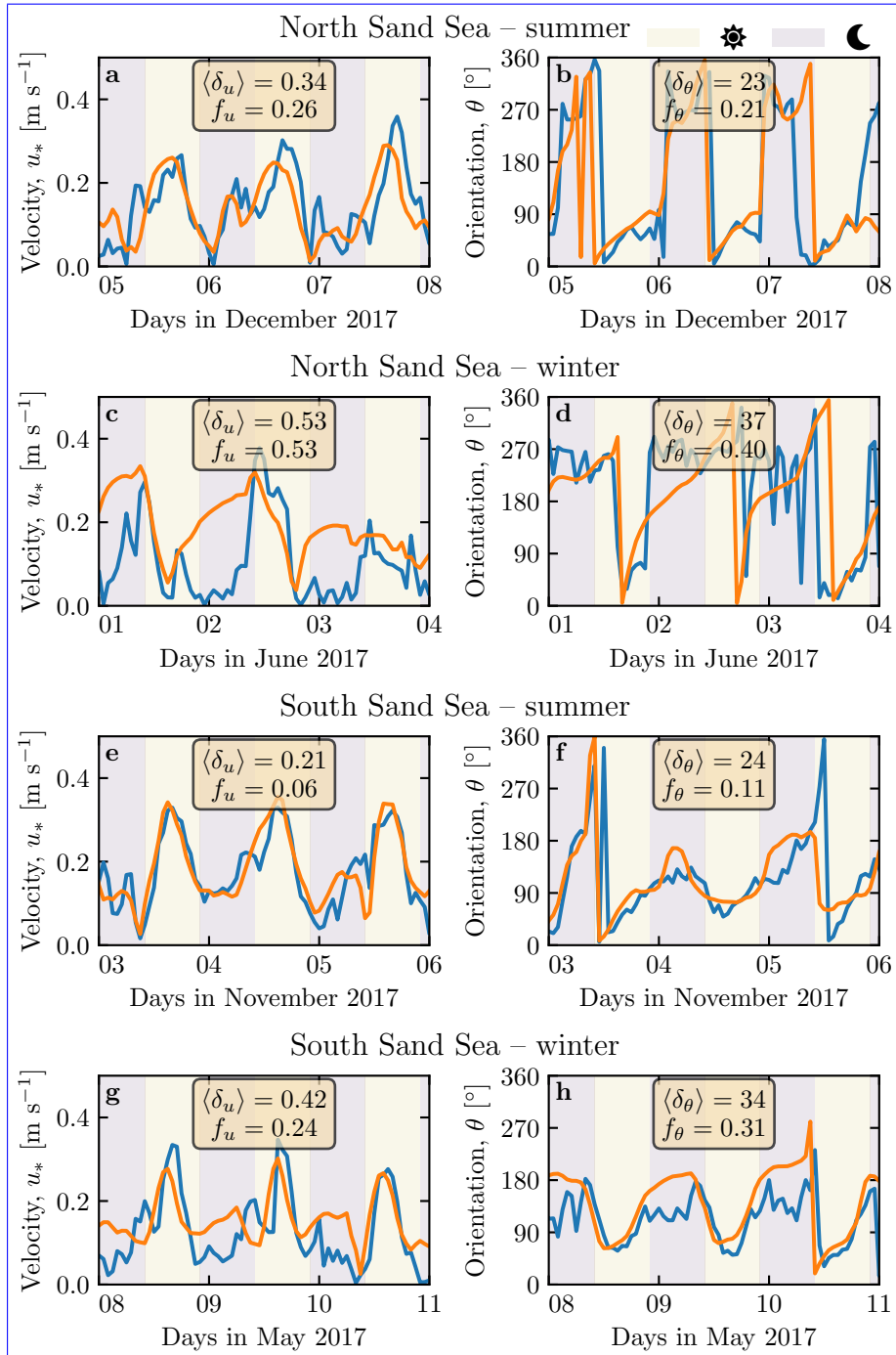


Fig. 5 Distributions of wind direction at Temporal comparison between the North Sand Sea Station for wind data coming from the ERA5-Land climate reanalysis (orange lines) and from the local measurements (blue lines). In each subplot, both distributions are plotted from the same time steps, selected with constraints on the wind direction. Coloured swatches indicate day (columns between 1000 UTC and 2200 UTC) and/or wind velocity night (rows before 1000 UTC or after 2200 UTC) of the ERA5-Land dataset. The grey vertical dashed lines indicate the dune orientation. The numbers at the top right give average flow deflection δ_θ and wind modulation δ_u over the percentage of time steps selected in each sub-range given period, as well as the percentage corresponding to the daytime (between 1000 UTC and 2200 UTC). The purple frame highlights the regime frequency of occurrence of extreme events (low wind velocities $\delta_\theta > 50^\circ$, nocturnal easterly wind $|\delta_u| > 0.6$). **a–b:** North Sand Sea station in which the data from both datasets differ summer. A similar figure can be obtained for the **b–c:** North Sand Sea station (Online Resource in winter, **d–e:** South Sand Sea in summer, **f–g:** South Sand Sea station in winter. Time series of the two other stations are shown in Fig. S8).

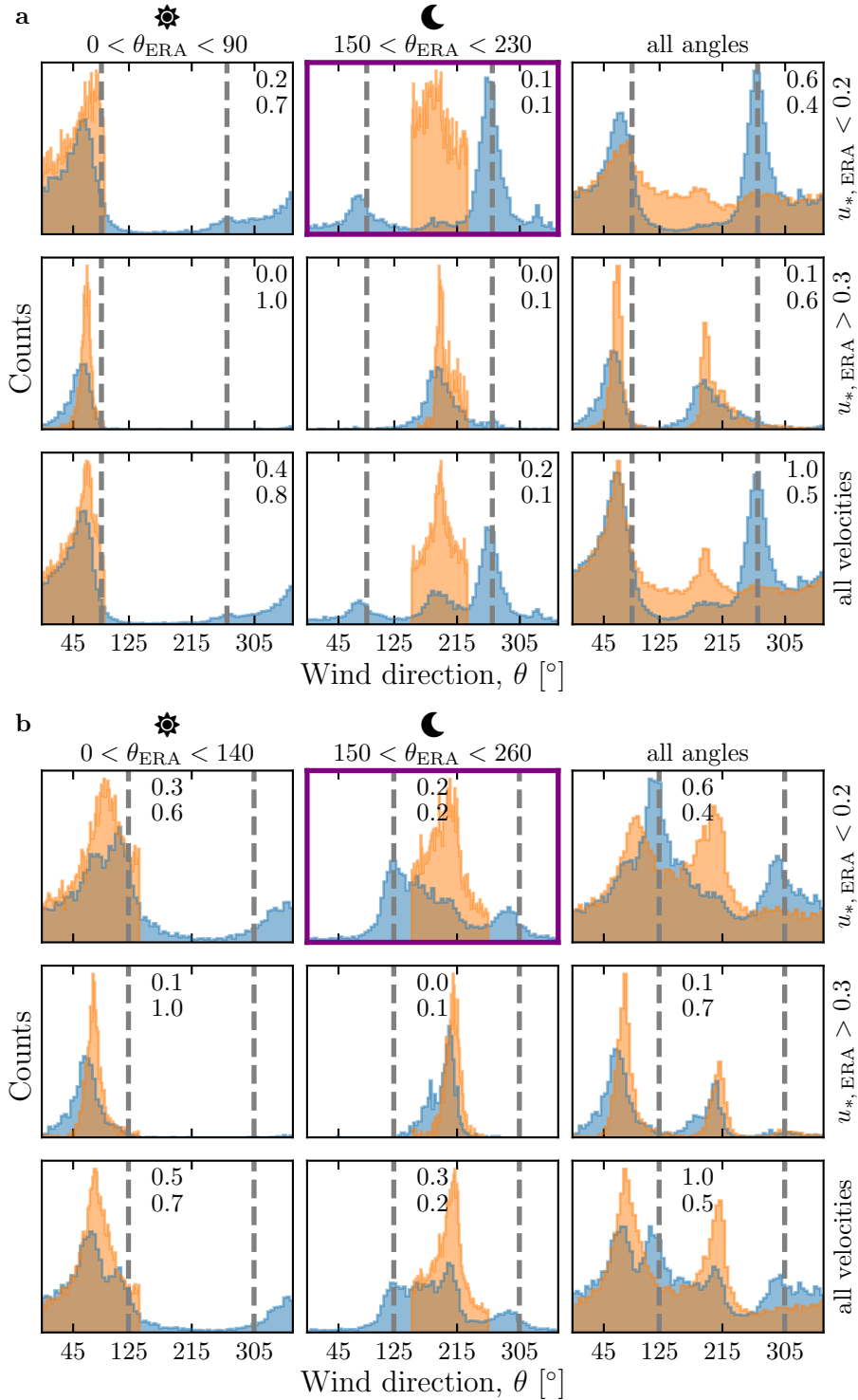


Fig. 6 Distributions of wind direction at the North Sand Sea (a) and South Sand Sea (b) stations for the ERA5-Land climate reanalysis (orange) and the local measurements (blue). In each subplot, both distributions are plotted from the same time steps, selected with constraints on the wind direction (columns) and/or wind velocity (rows) of the ERA5-Land dataset. The grey vertical dashed lines indicate the dune orientation. The numbers at the top right give the percentage of time steps selected in each sub-range, as well as the percentage corresponding to the daytime (between 1000 UTC and 2200 UTC). Contrary to the Huab and Etosha West stations (Fig. 4), histograms does not match low wind velocities. More specifically, the purple frame highlights the regime (low wind velocities, nocturnal easterly wind) in which the data from both datasets differ.

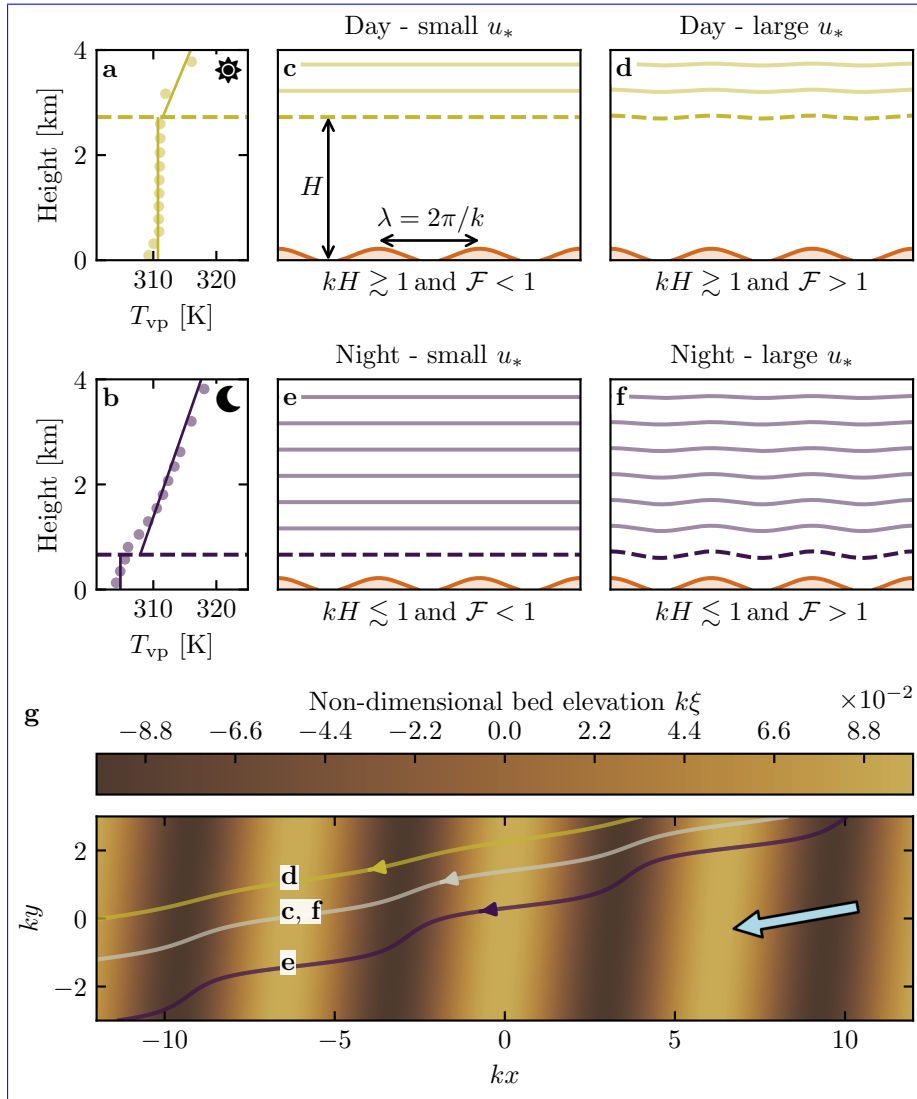


Fig. 7 **a–b:** Vertical profiles of the virtual potential temperature at 2 different time steps (day - 03/11/2015 - 1200 UTC, night - 01/13/2013 - 0900 UTC) at the North Sand Sea station. Dots: data from the ERA5 reanalysis. Dashed lines: boundary layer height given by the ERA5 reanalysis (Online Resource section 2). Plain lines: vertical (boundary layer) and linear (free atmosphere) fits to estimate the stratification properties. **c–f:** Sketches representing the interaction between the giant dunes and the atmospheric flow for different meteorological conditions. **g:** Streamlines over a sinusoidal topography $\xi(x, y)$ qualitatively representing the effect of low, medium and strong flow confinement, in relation to the above panels (see Appendix 1 for more details). The blue arrow indicates the undisturbed wind direction.

context an idealised bed elevation in the form of parallel sinusoidal ridges, with wavelength λ (or wavenumber $k = 2\pi/\lambda$) and amplitude ξ_0 , and where the reference flow direction makes a given incident angle with respect to the ridge crest (Andreotti et al. 2012). Part of this response, on which we focus here, is the flow deflection by the ridges. In a simplified way, it can be understood from the Bernoulli principle (Hesp et al. 2015): as the flow approaches the ridge crest, the compression of the streamlines results in larger flow velocities, and thus lower pressures ([Rubin and Hunter 1987](#)) ([Jackson and Hunt 1975](#)). An incident flow oblique to the ridge is then deflected towards lower pressure zones, i.e. towards the crest. Turbulent dissipation tends to increase this effect downstream, resulting in wind deflection along the crest in the lee side (Gadal et al. 2019).

Flow confinement below a capping surface, which enhances streamline compression, has a strong effect on the hydrodynamic response and typically increases flow deflection. This is the case for bedforms forming in open channel flows such as rivers ([Fourrière et al. 2010; Unsworth et al. 2018](#)) ([Kennedy 1963](#); [Chang and Simons 1970](#); [Mizumura 1995](#)). This is also relevant for aeolian dunes as they evolve in the turbulent atmospheric boundary layer (ABL) capped by the stratified free atmosphere (FA) (Andreotti et al. 2009). Two main mechanisms, associated with dimensionless numbers must then be considered (Fig. 47). First, topographic obstacles typically disturb the flow over a characteristic height similar to their length. As flow confinement is characterised by a thickness H , the interaction between the dunes and the wind in the ABL is well captured by the parameter kH . The height H is directly related to the radiative fluxes at the Earth surface. It is typically on the order of a kilometre, but significantly varies with the circadian and seasonal cycles. Emerging and small dunes, with wavelengths in the range 20 to 100 m, are not affected by the confinement, corresponding to $kH \gg 1$. For giant dunes with kilometric wavelengths, however, their interaction with the FA is significant (Andreotti et al. 2009). This translates into a parameter kH in the range 0.02–5, depending on the moment of the day and the season. A second important mechanism is associated with the existence of a thin intermediate so-called capping layer between the ABL and the FA. It is characterised by a density jump $\Delta\rho$, which controls the ‘rigidity’ of this interface, i.e. how much its deformation affects streamline compression. This is usually quantified using the Froude number (Vosper 2004; Stull 2006; Sheridan and Vosper 2006; Hunt et al. 2006; Jiang 2014):

$$\mathcal{F} = \frac{U}{\sqrt{\frac{\Delta\rho}{\rho_0} g H}}, \quad (1)$$

where U is the wind velocity at the top of the ABL and ρ_0 its average density. The intensity of the stratification, i.e. the amplitude of the gradient $|\partial_z \rho|$, also impacts its ability to deform the capping layer under the presence of an underlying obstacle, and thus affects the influence of flow confinement. This can be quantified using the internal Froude number (Vosper 2004; Stull 2006; Sheridan and Vosper 2006; Hunt et al. 2006; Jiang 2014) $\mathcal{F}_I = kU/N$, where

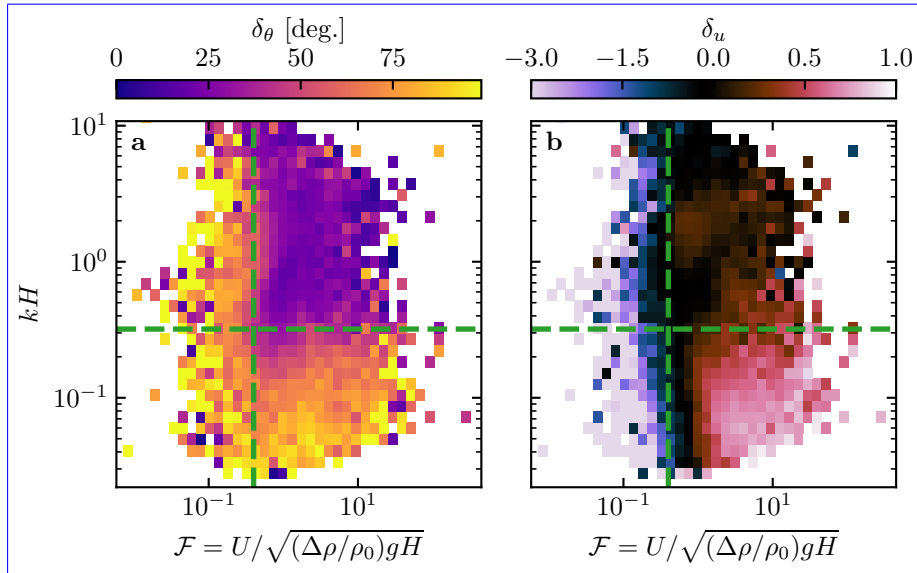


Fig. 8 Regime diagrams of the wind deviation δ_θ (a) and relative attenuation/amplification δ_u (b) in the space (\mathcal{F}, kH) , containing the data from both the North Sand Sea and South Sand Sea stations. Green dashed lines empirically delimit the different regimes. The point density in each bin of the diagrams is shown in Online Resource Fig. S14–S10 – 95% of the data occur in the range $-1 < \delta u < 1$. Similar regime diagrams in the spaces (\mathcal{F}_I, kH) and $(\mathcal{F}_I, \mathcal{F})$ are shown in Online Resource Fig. S11.

279 $N = \sqrt{-g\partial_z\rho/\rho_0}$ is the Brunt-Väisälä frequency (Stull 1988). Both Froude
280 numbers have in practice the same qualitative effect on flow confinement, and
281 we shall restrict the main discussion to \mathcal{F} only.

282 With this theoretical framework in mind, and in the context of the measured
283 wind data in the North and South Sand Sea stations, the smallest wind
284 disturbances are expected to occur during the day, when the ABL depth is the
285 largest and comparable to the dune wavelength ($kH \gtrsim 1$), which corresponds
286 to a weak confinement situation (Fig. 47c,d). In contrast, large wind disturbances
287 are expected to occur during the night, when the confinement is mainly
288 induced by a shallow ABL (Fig. 47e). However, this strong confinement can be
289 somewhat reduced in the case of strong winds, corresponding to large values of
290 the Froude number and a less ‘rigid’ interface (Fig. 47f). This is in qualitative
291 agreement with the transition from deflected to non-deflected winds related to
292 low and high velocities observed in our data (Sec. 2.2).

293 3.2 Data distribution in the flow regimes

294 We can go one step further and analyse how our data quantitatively spread
295 over the different regimes discussed above. For that purpose, one needs to
296 compute kH and \mathcal{F} from the time series. H , U and the other atmospheric

parameters can be deduced from the various vertical profiles (temperature, humidity) available in the ERA5 climate reanalysis (Online Resource section 2). We quantify the flow deflection δ_θ as the minimal angle between the wind orientations comparing the local measurements and the regional predictions. We also compute the relative velocity modulation as

$$\delta_u = \frac{u_*^{\text{ERA}} - u_*^{\text{station}}}{u_*^{\text{ERA}}}. \quad (2)$$

These two quantities are represented as maps in the plane (\mathcal{F}, kH) (Fig. 58a,b), and one can clearly identify different regions in these graphs. Small wind disturbances (small δ_θ and δ_u) are located in the top-right part of the diagrams, corresponding to a regime with low-interaction as well as low-confinement (kH and \mathcal{F} large enough, Fig. 47d). Lower values of kH (stronger interaction) or of Froude number (stronger confinement) both lead to an increase in wind disturbances, both in terms of orientation and velocity. Below a crossover value $kH \simeq 0.3$, wind disturbance is less sensitive to the \mathcal{F} -value. This is probably due to enhanced non-linear effects linked to flow modulation by the obstacle when confinement is strong. The Froude number also controls a transition from damped to amplified wind velocities in the interdune, with a crossover around $\mathcal{F} \simeq 0.4$ (Fig. 58b). Such an amplification is rather unexpected. Checking the occurrence of the corresponding data, it appears that these amplifications are associated with the southerly sea breeze, and occur dominantly during the October-March period, when the other easterly wind is not present (Online Resource Fig. ??S12a–b). Furthermore, they occur less frequently during the afternoon, and more frequently at the end of the day (Online Resource Fig. ??S12c). This effect may be linked to a change in the flow behaviour in the lee side of the obstacles but further measurements are needed in order to assess the different possibilities (Baines 1995; Vosper 2004).

Note that, in the presented results, the only quantities depending on the choice of the hydrodynamic roughnesses (see Online Resource section 4) are the wind shear velocities, and as such the Froude number Fr and the relative velocity modulation δ_u . Considering the possible range of realistic roughnesses values (10^{-4}m to 10^{-5}), the uncertainty of velocities estimated using the law of the wall, and thus the Froude number, is at most 30. It is harder to quantify the error on the computation of δ_u considering the method used. However, Figure S14 shows that this choice has very little influence of the temporal variation of the relative velocity modulation, but can induce a global increase or decrease of its values. As such, it will not change the aspect of the regime diagram presented in Figure 8b, but may only change the δ_u -value at which the transition between regimes is observed (here taken as 0, dashed black green lines in Figure 8b).

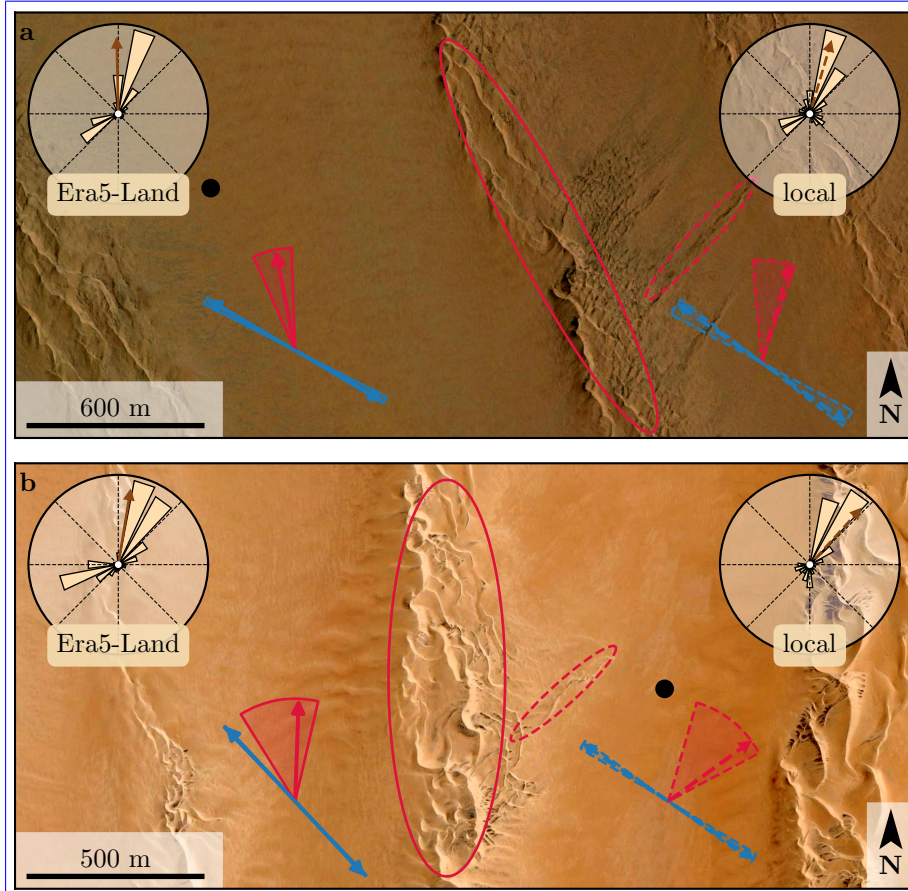


Fig. 9 Implications for smaller scale patterns in (a) the South Sand Sea and (b) North Sand Sea. The ellipses indicate the different types of elongating dunes, at large (plain line) and small (dashed line) scales. Dune orientation are predicted using the model of Courrech du Pont et al. (2014) from the sand flux angular distributions, shown here (roses and resultant transport direction) for typical values (grain size $180 \mu\text{m}$, flux-up ratio of 1.6). Code for corresponding arrows: use of ERA5-Land data (plain line), use of local measurements (dashed line), prediction for the bed instability growth mechanism (blue), prediction for the elongation growth mechanism (red). Wedges show the uncertainty on the orientation calculation when parameters are varied. The black dots indicate the location of the meteorological stations with respect to the dunes. See Appendix 2 for additional details.

335 4 Discussion and conclusion

336 The feedback of the giant dunes on the wind flow has important implications
 337 for smaller scales bedforms. As illustrated in Fig. 69, small linear dunes
 338 ($\sim 50 \text{ m}$ wide) are often present in the 1–2 km interdune between giant linear
 339 dunes in the Namib Sand Sea (Livingstone et al. 2010). These smaller dunes do
 340 not exhibit the same orientation as the large ones, and are sometimes named

‘crossing dunes’. Whilst differences between large and small scale dune patterns are observed ubiquitously, they are largely attributed to the presence of two different dune growth mechanisms, leading to two different dune patterns (orientations and/or morphologies) for the same wind regime (Courrech du Pont et al. 2014; Runyon et al. 2017; Lü et al. 2017; Song et al. 2019; Gadal et al. 2020; Hu et al. 2021). Here, however, our arguments enable the development of differing orientations for the small and giant linear dunes whilst also imposing the same dune growth mechanism (elongating mode). Figure 6 shows how the orientations for the small and giant dunes can be derived from the locally measured and regionally predicted winds respectively (red arrows in Fig. 69). These predictions require a specification for the threshold of eolian sand transport. Importantly, its value expressed as a shear velocity $u_{th} \simeq 0.15 \text{ ms}^{-1}$ is reached in the deflected wind regime already. The feedback of the giant dunes on the wind described in this study thus provides a potential explanation for the existence of these small linear dunes elongating across the interdune, a dynamic which has remained unresolved to date. These crossing dunes could provide additional constraints for the inference of local winds from bedforms, similarly to that currently performed on Mars using ripple orientations (Liu and Zimbelman 2015; Hood et al. 2021). Further work is needed to investigate these processes in more detail, including measurements of sediment transport and flow on the top of dunes.

This study presents the evidence that wind flow patterns around giant dunes are influenced by the atmospheric boundary layer, particularly during nocturnal conditions. It leaves open the debate as to whether the size of giant dunes is limited by the depth of this layer (Andreotti et al. 2009), in contrast to an unconstrained dune growth, ever-slower with size (Gunn et al. 2021a). More field evidence is needed from additional dune fields, but this mechanism would then allow for the inference of the ABL depth from giant bedform wavelengths where measurements are not feasible or available, such as Titan (Lorenz et al. 2010).

To conclude on conditions under which the ERA5-Land reanalysis data can reliably be used to study dune morphodynamics, we summarise the comparison of local (direct measurements) and regional (climate reanalysis) wind data. In flat areas, the agreement between the two confirms the ability of the ERA5-Land climate reanalysis to predict the wind regime down to scales $\sim 10 \text{ km}$, i.e the model grid. When smaller scale topographies are present (giant dunes in our case), locally measured winds can significantly differ from the regionally predicted ones. This is the case when the disturbances induced by the dunes interact with the lower part of the ABL vertical structure, which presents circadian variations. During the day, when the capping layer is typically high, this interaction is small, and the ERA5-Land predictions are also quantitatively consistent with the local data. During the night, however, the presence of a shallow atmospheric boundary layer induces a strong confinement of the flow, and is associated with large wind deflection by the dunes. Importantly, we find that this effect can be counterbalanced for large wind velocities, which

386 are capable of deforming the capping layer, thus decreasing the influence of
387 the confinement.

388 The theoretical computation of the wind disturbances induced by simu-
389 sigmoidal ridges under flow confinement has been performed in the linear limit
390 (Andreotti et al. 2009, 2012), i.e. when the aspect ~~ration~~ratio of these ridges
391 is small ($k\xi_0 \ll 1$). These models are able to qualitatively reproduce the ob-
392 served wind deflection (Appendix 1, Online Resource Figs. ?? and ??S11 and
393 S13), and thus provide the physical support for the interpretation we propose
394 here based on hydrodynamic regimes. However, these models cannot quan-
395 titatively predict the magnitude of these observations, probably due to the
396 presence of expected non-linearities in high confinement situations linked to
397 strong flow modulations. Besides, these linear calculations only predict wind
398 attenuation in the interdune, in contrast with the observed enhanced veloc-
399 ities associated with particular evening winds from the South during the period
400 October–March (Online Resource Fig. ??S12). Some other models predict dif-
401 ferent spatial flow structures in response to a modulated topography, such as
402 lee waves and rotors (Baines 1995; Vosper 2004). However, our measurements
403 are located at a single point in the interdune, so we are unable to explore
404 these types of responses. Data at different places along and across the ridges
405 are needed to investigate and possibly map such flow structures, and for further
406 comparisons with the models.

407 **Acknowledgements** We would like to acknowledge the contributors of the following open-
408 source python libraries, Matplotlib (Hunter 2007), Numpy (Harris et al. 2020) and Scipy
409 (Virtanen et al. 2020), which provide an incredibly efficient ecosystem allowing scientific
410 research in Python.

411 All data used in this study can be found in Gadale et al. (2022). Note that it contains
412 modified Copernicus Climate Change Service Information (2021). Neither the European
413 Commission nor ECMWF is responsible for any use that may be made of the Copernicus
414 Information or Data it contains. Fully documented codes used to analyse this study are
415 available at <https://github.com/Cgadal/GiantDunes> (will be made public upon acceptance
416 of this manuscript for publication).

417 Multiple grants have supported the collection of wind data through visits to the four
418 sites between 2013 and 2020 (John Fell Oxford University Press (OUP) Research Fund
419 (121/474); National Geographic (CP-029R-17); Natural Environment Research Council UK
420 (NE/R010196/1 and NE/H021841/1 NSFGEO-NERC); Southampton Marine and Maritime
421 Institute SMMI EPSRC-GCRF UK), along with research permits (1978/2014, 2140/2016,
422 2304/2017, 2308/2017, RPIV00022018, RPIV0052018, RPIV00230218). The authors are
423 very grateful for support from Etosha National Park (especially Shyane Kötting, Boas Er-
424 ckie, Pierre du Preez, Claudine Cloete, Immanuel Kapofi, Wilferd Versfeld, and Werner
425 Kilian), Gobabeb Namib Research Institute (Gillian Maggs-Kölling and Eugene Marais),
426 The Skeleton Coast National Park (Joshua Kazeurua). Various researchers and desert en-
427 thusiasts have assisted with instruments and the logistics of expeditions, especially Mary
428 Seely for expert guidance at the North Sand Sea site.

429 Finally, we acknowledge financial support from the Laboratoire d'Excellence UnivEarthS
430 Grant ANR-10-LABX-0023, the Initiative d'Excellence Université de Paris Grant ANR-18-
431 IDEX-0001, the French National Research Agency Grants ANR-17-CE01-0014/SONO and
432 the National Science Center of Poland Grant 2016/23/B/ST10/01700.

433 **Appendix 1: Linear theory of wind response to topographic pertur-**
434 **bation**

435 Following the work of Fourrière et al. (2010), Andreotti et al. (2012) and
436 Andreotti et al. (2009), we briefly describe in this appendix the framework
437 for the linear response of a turbulent flow to a topographic perturbation of
438 small aspect ratio. As a general bed elevation can be decomposed into Fourier
439 modes, we focus here on a sinusoidal topography:

$$\xi = \xi_0 \cos [k (\cos(\alpha)y - \sin(\alpha)x)], \quad (3)$$

440 which is also a good approximation for the giant dunes observed in the North
441 Sand Sea and South Sand Sea Station (Fig. 1–2 and Online Resource Fig. S5–S4).
442 Here, x and y are the streamwise and spanwise coordinates, $k = 2\pi/\lambda$ the
443 wavenumber of the sinusoidal perturbation, α its crest orientation with respect
444 to the x -direction (anticlockwise) and ξ_0 its amplitude. The two components
445 of the basal shear stress $\tau = \rho_0 u_* \mathbf{u}_*$, constant in the flat bottom reference
446 case, can then be generically written as:

$$\tau_x = \tau_0 \left(1 + k\xi_0 \sqrt{\mathcal{A}_x^2 + \mathcal{B}_x^2} \cos [k (\cos(\alpha)y - \sin(\alpha)x) + \phi_x] \right), \quad (4)$$

$$\tau_y = \tau_0 k\xi_0 \sqrt{\mathcal{A}_y^2 + \mathcal{B}_y^2} \cos [k (\cos(\alpha)y - \sin(\alpha)x) + \phi_y], \quad (5)$$

447 where τ_0 is the reference basal shear stress on a flat bed. We have defined
448 the phase $\phi_{x,y} = \tan^{-1}(\mathcal{B}_{x,y}/\mathcal{A}_{x,y})$ from the in-phase and in-quadrature hy-
449 drodynamical coefficients $\mathcal{A}_{x,y}$ and $\mathcal{B}_{x,y}$. They are functions of k and of the
450 flow conditions, i.e the bottom roughness, the vertical flow structure and the
451 incident flow direction, and the theoretical framework developed in the above
452 cited papers proposes methods to compute them in the linear regime.

453 Following Andreotti et al. (2012), the effect of the incident wind direction
454 can be approximated by the following expressions:

$$\mathcal{A}_x = \mathcal{A}_0 \sin^2 \alpha, \quad (6)$$

$$\mathcal{B}_x = \mathcal{B}_0 \sin^2 \alpha, \quad (7)$$

$$\mathcal{A}_y = -\frac{1}{2} \mathcal{A}_0 \cos \alpha \sin \alpha, \quad (8)$$

$$\mathcal{B}_y = -\frac{1}{2} \mathcal{B}_0 \cos \alpha \sin \alpha, \quad (9)$$

455 where \mathcal{A}_0 and \mathcal{B}_0 are now two coefficients independent of the dune orientation
456 α , corresponding to the transverse case ($\alpha = 90^\circ$). For In the case of a fully
457 turbulent boundary layer capped by a stratified atmosphere, these coefficients
458 depend on kH , kz_0 , \mathcal{F} and \mathcal{F}_1 (Andreotti et al. 2009). In this study For their
459 computation, we assume here a constant hydrodynamic roughness $z_0 \simeq 1$ mm
460 (Online Resource section 1). For the considered giant dunes, this leads to
461 $kz_0 \simeq 2 \cdot 10^{-6}$, as their wavelength is $\lambda \simeq 2.4$ km (or $k \simeq 2 \cdot 10^{-3} \text{ m}^{-1}$). Values
462 of z_0 extracted from field data indeed typically fall between 0.1 mm and 10

463 mm (Sherman and Farrell 2008; Field and Pelletier 2018). Importantly, \mathcal{A}_0
 464 and \mathcal{B}_0 do not vary much in the corresponding range of kz_0 (Fourrière et al.
 465 2010), and the results presented here are robust with respect to this choice.

466 With capping layer height and Froude numbers computed from the ERA5-
 467 Land time series, the corresponding \mathcal{A}_0 and \mathcal{B}_0 can be deduced, as displayed
 468 in Online Resource Fig. ??S13. Interestingly, it shows similar regimes as in
 469 the diagrams of Fig. 5.8 and Online Resource Fig. ??S11a,b, supporting the
 470 underlying physics. However, the agreement is qualitative only. Further, the
 471 linearity assumption of the theoretical framework requires $(|\tau| - \tau_0) / \tau_0 \ll 1$,
 472 which translates into $k\xi\sqrt{\mathcal{A}_0^2 + \mathcal{B}_0^2} \ll 1$. In our case, the giant dune morphol-
 473 ogy gives $k\xi_0 \simeq 0.1$, which means that one quits the regime of validity of the
 474 linear theory when the coefficient modulus $\sqrt{\mathcal{A}_0^2 + \mathcal{B}_0^2}$ becomes larger than a
 475 few units. In accordance with the theoretical expectations, these coefficients
 476 present values on the order of unity ($\mathcal{A}_0 \simeq 3$ and $\mathcal{B}_0 \simeq 1$) in unconfined situa-
 477 tions (Claudin et al. 2013; Lü et al. 2021). In contrast and as illustrated in
 478 Online Resource Fig. ??S13a,b, larger values are predicted in case of strong
 479 confinement, which does not allow us to proceed to further quantitative com-
 480 parison with the data.

481 Finally, the linear model is also able to reproduce the enhancement of
 482 the flow deflection over the sinusoidal ridges when $\sqrt{\mathcal{A}_0^2 + \mathcal{B}_0^2}$ is increased
 483 (Online Resource Fig. ??S13). Here, using $k\xi_0 \simeq 0.1$ to be representative of
 484 the amplitude of the giant dunes at the North Sand Sea station, the coefficient
 485 modulus is bounded to 10.

486 Appendix 2: Sediment transport and dune morphodynamics

487 We summarise in this appendix the sediment transport and dune morphody-
 488 namics theoretical framework leading to the prediction of sand fluxes and dune
 489 orientations from wind data.

490 *Sediment transport* — The prediction of sand fluxes from wind data has been
 491 a long standing issue in aeolian geomorphological studies (Fryberger and Dean
 492 1979; Pearce and Walker 2005; Sherman and Li 2012; Shen et al. 2019). Based
 493 on laboratory studies in wind tunnels (Rasmussen et al. 1996; Iversen and
 494 Rasmussen 1999; Creysse et al. 2009; Ho et al. 2011), as well as physical
 495 considerations (Ungar and Haff 1987; Andreotti 2004; Durán et al. 2011; Páhtz
 496 and Durán 2020), it has been shown that the steady saturated saltation flux
 497 over a flat sand bed depends linearly on the shear stress:

$$\frac{q_{\text{sat}}}{Q} = \Omega \sqrt{\Theta_{\text{th}}} (\Theta - \Theta_{\text{th}}), \quad (10)$$

498 where Ω is a proportionality constant, $Q = d\sqrt{(\rho_s - \rho_0)gd/\rho_0}$ is a character-
 499 istic flux, $\Theta = \rho_0 u_*^2 / (\rho_s - \rho_0)gd$ the Shields number, and Θ_{th} its threshold
 500 value below which saltation vanishes. $\rho_s = 2.6 \text{ g cm}^{-3}$ and $d = 180 \mu\text{m}$ are
 501 the grain density and diameter, and g is the gravitational acceleration. The

shear velocity, and consequently the Shields number as well as the sediment flux, are time dependent.

Recently, Pähzt and Durán (2020) suggested an additional quadratic term in Shields to account for grain-grain interactions within the transport layer at strong wind velocities:

$$\frac{q_{\text{sat}, t}}{Q} = \frac{2\sqrt{\Theta_{\text{th}}}}{\kappa\mu} (\Theta - \Theta_{\text{th}}) \left(1 + \frac{C_M}{\mu} [\Theta - \Theta_{\text{th}}] \right), \quad (11)$$

where $\kappa = 0.4$ is the von Kármán constant, $C_M \simeq 1.7$ a constant and $\mu \simeq 0.6$ is a friction coefficient, taken to be the avalanche slope of the granular material. The fit of this law to the experimental data of Creyssels et al. (2009) and Ho et al. (2011) gives $\Theta_{\text{th}} = 0.0035$. The fit of Eq. 10 on these same data similarly gives $\Omega \simeq 8$ and $\Theta_{\text{th}} = 0.005$. The sand flux angular distributions and the dune orientations in Fig. 6-9 are calculated using this law (11). We have checked that using the ordinary linear relationship (10) instead does not change the predicted dune orientations by more than a few degrees.

Dune orientations — Dune orientations are predicted with the dimensional model of Courrech du Pont et al. (2014), from the sand flux time series computed with the above transport law. Two orientations are possible depending on the mechanism dominating the dune growth: elongation or bed instability. The orientation α corresponding the bed instability is then the one that maximises the following growth rate (Rubin and Hunter 1987):

$$\sigma \propto \frac{1}{H_d W_d T} \int_0^T q_{\text{crest}} |\sin(\theta - \alpha)| dt, \quad (12)$$

where θ is the wind orientation measured with respect to the same reference as α , and H_d and W_d are dimensional constants respectively representing the dune height and width. The integral runs over a time T , which must be representative of the characteristic period of the wind regime. The flux at the crest is expressed as:

$$q_{\text{crest}} = q_{\text{sat}} [1 + \gamma |\sin(\theta - \alpha)|], \quad (13)$$

where the flux-up ratio γ has been calibrated to 1.6 using field studies, underwater laboratory experiments and numerical simulations. Predictions of the linear analysis of Gadal et al. (2019) and Delorme et al. (2020) give similar results.

Similarly, the dune orientation corresponding to the elongation mechanism is the one that verifies:

$$\tan(\alpha) = \frac{\langle q_{\text{crest}}(\alpha) \mathbf{e}_\theta \rangle \cdot \mathbf{e}_{WE}}{\langle q_{\text{crest}}(\alpha) \mathbf{e}_\theta \rangle \cdot \mathbf{e}_{SN}}, \quad (14)$$

where $\langle \cdot \rangle$ denotes a vectorial time average. The unitary vectors \mathbf{e}_{WE} , \mathbf{e}_{SN} and \mathbf{e}_θ are in the West-East, South-North and wind directions, respectively.

The resulting computed dune orientations, blue and red arrows in Fig. 6-9, then depend on a certain number of parameters (grain properties, flux-up ratio,

536 etc.), for which we take typical values for aeolian sandy deserts. Due to the lack
537 of measurements in the studied places, some uncertainties can be expected. We
538 therefore run a sensitivity test by calculating the dune orientations for grain
539 diameters ranging from 100 μm to 400 μm and for a speed-up ratio between
540 0.1 and 10 (wedges in Fig. 69).

References

- 542 Andreotti B (2004) A two-species model of aeolian sand transport. *J Fluid
543 Mech* 510:47–70
- 544 Andreotti B, Claudin P, Douady S (2002) Selection of dune shapes and veloc-
545 ities part 1: Dynamics of sand, wind and barchans. *The European Physical
546 Journal B-Condensed Matter and Complex Systems* 28(3):321–339
- 547 Andreotti B, Fourrière A, Ould-Kaddour F, Murray B, Claudin P (2009) Gi-
548 ant aeolian dune size determined by the average depth of the atmospheric
549 boundary layer. *Nature* 457:1120–1123
- 550 Andreotti B, Claudin P, Devauchelle O, Durán O, Fourrière A (2012) Bedforms
551 in a turbulent stream: ripples, chevrons and antidunes. *J Fluid Mech* 690:94–
552 128
- 553 Ashkenazy Y, Yizhaq H, Tsoar H (2012) Sand dune mobility under climate
554 change in the kalahari and australian deserts. *Climatic Change* 112:901–923
- 555 Baddock M, Livingstone I, Wiggs G (2007) The geomorphological significance
556 of airflow patterns in transverse dune interdunes. *Geomorphology* 87:322–
557 336
- 558 Bagnold RA (1941) *The Physics of Blown Sand and Desert Dunes*. London :
559 Methuen : Chapman & Hall
- 560 Baines PG (1995) Topographic effects in stratified flows. Cambridge university
561 press
- 562 Bauer BO, Sherman DJ, Wolcott JF (1992) Sources of uncertainty in shear
563 stress and roughness length estimates derived from velocity profiles. *The
564 Professional Geographer* 44:453–464
- 565 Belcher S, JCR H (1998) Turbulent flow over hills and waves. *Annu Rev Fluid
566 Mech* 30:507–538
- 567 Blumberg DG, Greeley R (1996) A comparison of general circulation model
568 predictions to sand drift and dune orientations. *J Clim* 9:3248–3259
- 569 Bristow NR, Best J, Wiggs GFS, Nield JM, Baddock MC, Delorme P, Chris-
570 tensen KT (2022) Topographic perturbation of turbulent boundary layers
571 by low-angle, early-stage aeolian dunes. *Earth Surf Process Landf* n/a(n/a),
572 DOI <https://doi.org/10.1002/esp.5326>
- 573 Brookfield M (1977) The origin of bounding surfaces in ancient aeolian sand-
574 stones. *Sedimentology* 24(3):303–332
- 575 Brown S, Nickling WG, Gillies JA (2008) A wind tunnel examination of shear
576 stress partitioning for an assortment of surface roughness distributions. *J
577 Geophys Res* 113:F02S06
- 578 Chang H, Simons D (1970) The bed configuration of straight sand-bed channels
579 when flow is nearly critical. *J Fluid Mech* 42(3):491–495
- 580 Charru F, Andreotti B, Claudin P (2013) Sand ripples and dunes. *Annu Rev
581 Fluid Mech* 45:469–493
- 582 Claudin P, Wiggs G, Andreotti B (2013) Field evidence for the upwind velocity
583 shift at the crest of low dunes. *Boundary-Layer Meteorol* 148:195–206
- 584 Claudin P, Durán O, Andreotti B (2017) Dissolution instability and roughen-
585 ing transition. *J Fluid Mech* 832:R2

- 586 Claudin P, Louge M, Andreotti B (2021) Basal pressure variations induced by
587 a turbulent flow over a wavy surface. *Frontiers in Physics* 9:682564
- 588 Colombini M (2004) Revisiting the linear theory of sand dune formation. *J
589 Fluid Mech* 502:1–16
- 590 Courrech du Pont S (2015) Dune morphodynamics. *C R Phys* 16:118–138
- 591 Courrech du Pont S, Narteau C, Gao X (2014) Two modes for dune orientation.
592 *Geology* 42:743–746
- 593 Creyssels M, Dupont P, El Moctar AO, Valance A, Cantat I, Jenkins JT, Pasini
594 JM, Rasmussen KR (2009) Saltating particles in a turbulent boundary layer:
595 experiment and theory. *J Fluid Mech* 625:47–74
- 596 de Winter W, Donker J, Sterk G, Van Beem J, Ruessink G (2020) Regional
597 versus local wind speed and direction at a narrow beach with a high and
598 steep foredune. *Plos one* 15(1):e0226983
- 599 Dee DP, Uppala SM, Simmons AJ, Berrisford P, Poli P, Kobayashi S, Andrae
600 U, Balmaseda M, Balsamo G, Bauer dP, et al. (2011) The era-interim re-
601 analysis: Configuration and performance of the data assimilation system. *Q
602 J R Meteorol Soc* 137:553–597
- 603 Delorme P, Wiggs G, Baddock M, Claudin P, Nield J, Valdez A (2020) Dune
604 initiation in a bimodal wind regime. *J Geophys Res* 125:e2020JF005757
- 605 Durán O, Claudin P, Andreotti B (2011) On aeolian transport: Grain-scale
606 interactions, dynamical mechanisms and scaling laws. *Aeolian Res* 3:243–
607 270
- 608 Durran DR (1990) Mountain waves and downslope winds. In: *Atmospheric
609 processes over complex terrain*, Springer, pp 59–81
- 610 Dyer A (1974) A review of flux-profile relationships. *Boundary-Layer Meteorol
611* 7(3):363–372
- 612 Ewing RC, Kocurek G, Lake LW (2006) Pattern analysis of dune-field param-
613 eters. *Earth Surf Process Landf* 31(9):1176–1191
- 614 Farr TG, Rosen PA, Caro E, Crippen R, Duren R, Hensley S, Kobrick M,
615 Paller M, Rodriguez E, Roth L, et al. (2007) The shuttle radar topography
616 mission. *Rev Geophys* 45
- 617 Fernando H, Mann J, Palma J, Lundquist JK, Barthelmie RJ, Belo-Pereira M,
618 Brown W, Chow F, Gerz T, Hocut C, et al. (2019) The perdigão: Peering
619 into microscale details of mountain winds. *Bull Am Meteorol Soc* 100:799–
620 819
- 621 Field JP, Pelletier JD (2018) Controls on the aerodynamic roughness length
622 and the grain-size dependence of aeolian sediment transport. *Earth Surf
623 Process Landf* 43:2616–2626
- 624 Finnigan J, Raupach M, Bradley E, Aldis G (1990) A wind tunnel study
625 of turbulent flow over a two-dimensional ridge. *Boundary-Layer Meteorol
626* 50:277–317
- 627 Finnigan J, Ayotte K, Harman I, Katul G, Oldroyd H, Patton E, Poggi D,
628 Ross A, Taylor P (2020) Boundary-layer flow over complex topography.
629 *Boundary-Layer Meteorol* 177:247–313
- 630 Flack K, Schultz M (2010) Review of hydraulic roughness scales in the fully
631 rough regime. *Journal of Fluids Engineering* 132:041203

- 632 Fourrière A, Claudin P, Andreotti B (2010) Bedforms in a turbulent stream:
633 formation of ripples by primary linear instability and of dunes by nonlinear
634 pattern coarsening. *J Fluid Mech* 649:287–328
- 635 Frederick KA, Hanratty TJ (1988) Velocity measurements for a turbulent non-
636 separated flow over solid waves. *Exp Fluids* 6:477–486
- 637 Fryberger SG, Dean G (1979) Dune forms and wind regime. A study of global
638 sand seas 1052:137–169
- 639 Gadal C, Narteau C, Courrech Du Pont S, Rozier O, Claudin P (2019) Incip-
640 ient bedforms in a bidirectional wind regime. *J Fluid Mech* 862:490–516
- 641 Gadal C, Narteau C, Courrech du Pont S, Rozier O, Claudin P (2020) Peri-
642 odicity in fields of elongating dunes. *Geology* 48:343–347
- 643 Gadal C, Delorme P, Narteau C, Wiggs G, Baddock M, Nield JM, Claudin
644 P (2022) Data used in 'Local wind regime induced by giant linear dunes:
645 comparison of ERA5-Land re-analysis with surface measurements'. DOI
646 10.5281/zenodo.6343138
- 647 Garratt JR (1994) The atmospheric boundary layer. *Earth-Science Reviews*
648 37(1-2):89–134
- 649 Garvey B, Castro IP, Wiggs G, Bullard J (2005) Measurements of flows over
650 isolated valleys. *Boundary-Layer Meteorol* 117(3):417–446
- 651 Gong W, Ibbetson A (1989) A wind tunnel study of turbulent flow over model
652 hills. *Boundary-Layer Meteorol* 49:113–148
- 653 Gong W, Taylor P, Dörnbrack A (1996) Turbulent boundary-layer flow over
654 fixed aerodynamically rough two-dimensional sinusoidal waves. *J Fluid Mech*
655 312:1–37
- 656 Guérin A, Derr J, Du Pont SC, Berhanu M (2020) Streamwise dissolution
657 patterns created by a flowing water film. *Phys Rev Lett* 125(19):194502
- 658 Gunn A, Casasanta G, Di Liberto L, Falcini F, Lancaster N,
659 Jerolmack DJ (2021a) What sets aeolian dune height? DOI
660 <https://doi.org/10.31223/X5QG8S>
- 661 Gunn A, Wanker M, Lancaster N, Edmonds D, Ewing R, Jerolmack
662 D (2021b) Circadian rhythm of dune-field activity. *Geophys Res Lett*
663 48:e2020GL090924
- 664 Harris CR, Millman KJ, van der Walt SJ, Gommers R, Virtanen P, Cournapeau D,
665 Wieser E, Taylor J, Berg S, Smith NJ, et al. (2020) Array program-
666 ming with numpy. *Nature* 585:357–362
- 667 Havholm KG, Kocurek G (1988) A preliminary study of the dynamics of
668 a modern draa, algodones, southeastern california, usa. *Sedimentology*
669 35(4):649–669
- 670 Hersbach H, Bell B, Berrisford P, Hirahara S, Horányi A, Muñoz-Sabater J,
671 Nicolas J, Peubey C, Radu R, Schepers D, et al. (2020) The era5 global
672 reanalysis. *Q J R Meteorol Soc* 146:1999–2049
- 673 Hesp P, Illenberger W, Rust I, McLachlan A, Hyde R (1989) Some aspects of
674 transgressive dunefield and transverse dune geomorphology and dynamics,
675 south coast, south africa. *Zeitschrift fur Geomorphologie*, Supplementband
676 73:111–123

- 677 Hesp PA, Hastings K (1998) Width, height and slope relationships and aero-
678 dynamic maintenance of barchans. *Geomorphology* 22(2):193–204
- 679 Hesp PA, Smyth TAG, Nielsen P, Walker IJ, Bauer BO, Davidson-Arnott R
680 (2015) Flow deflection over a foredune. *Geomorphology* 230:64–74
- 681 Ho TD, Valance A, Dupont P, Ould El Moctar A, Tuan Duc H, Valance A,
682 Dupont P, Ould El Moctar A (2011) Scaling laws in aeolian sand transport.
683 *Phys Rev Lett* 106:4–7
- 684 Hood DR, Ewing RC, Roback KP, Runyon K, Avouac JP, McEnroe M (2021)
685 Inferring airflow across martian dunes from ripple patterns and dynamics.
686 *Frontiers in Earth Science* 9:702828
- 687 Howard AD (1977) Effect of slope on the threshold of motion and its applica-
688 tion to orientation of wind ripples. *Geological Society of America Bulletin*
689 88:853–856
- 690 Hu Z, Gao X, Lei J, Zhou N (2021) Geomorphology of aeolian dunes in the
691 western sahara desert. *Geomorphology* 392:107916
- 692 Hunt J, Leibovich S, Richards K (1988) Turbulent shear flows over low hills.
693 *Q J R Meteorol Soc* 114:1435–1470
- 694 Hunt JCR, Vilenski GG, Johnson ER (2006) Stratified separated flow around
695 a mountain with an inversion layer below the mountain top. *J Fluid Mech*
696 556:105–119
- 697 Hunter JD (2007) Matplotlib: A 2d graphics environment. *Computing in sci-
698 ence & engineering* 9:90–95
- 699 Iversen JD, Rasmussen KR (1999) The effect of wind speed and bed slope on
700 sand transport. *Sedimentology* 46:723–731
- 701 Jackson PS, Hunt JCR (1975) Turbulent wind flow over a low hill. *Q J R
702 Meteorol Soc* 101:929–955
- 703 Jiang Q (2014) Applicability of reduced-gravity shallow-water theory to atmo-
704 spheric flow over topography. *J Atmos Sci* 71:1460–1479
- 705 Jolivet M, Braucher R, Dovchintseren D, Hocquet S, Schmitt J, ASTER Team
706 (2021) Erosion around a large-scale topographic high in a semi-arid sedimen-
707 tary basin: Interactions between fluvial erosion, aeolian erosion and aeolian
708 transport. *Geomorphology* 386:107747
- 709 Kennedy JF (1963) The mechanics of dunes and antidunes in erodible-bed
710 channels. *J Fluid Mech* 16(4):521–544
- 711 Kim HG, Patel VC, Lee CM (2000) Numerical simulation of wind flow over
712 hilly terrain. *J Wind Eng Ind Aerodyn* 87:45–60
- 713 Lancaster J, Lancaster N, Seely M (1984) Climate of the central namib desert.
714 *Madoqua* 1984:5–61
- 715 Lancaster N (1985) Winds and sand movements in the namib sand sea. *Earth
716 Surf Process Landf* 10:607–619
- 717 Lancaster N, Nickling W, Neuman CM, Wyatt V (1996) Sediment flux and
718 airflow on the stoss slope of a barchan dune. *Geomorphology* 17(1-3):55–62
- 719 Lewis HW, Mobbs SD, Lehning M (2008) Observations of cross-ridge flows
720 across steep terrain. *Q J R Meteorol Soc* 134:801–816
- 721 Liu ZYC, Zimbelman JR (2015) Recent near-surface wind directions inferred
722 from mapping sand ripples on martian dunes. *Icarus* 261:169–181

- 723 Livingstone I, Warren A (2019) Aeolian geomorphology: a new introduction.
724 Wiley
- 725 Livingstone I, Bristow C, Bryant RG, Bullard J, White K, Wiggs GFS, Baas
726 ACW, Bateman MD, Thomas DSG (2010) The namib sand sea digital
727 database of aeolian dunes and key forcing variables. *Aeolian Res* 2:93–104
- 728 Lorenz R, Claudin P, Andreotti B, Radebaugh J, Tokano T (2010) A 3 km
729 atmospheric boundary layer on titan indicated by dune spacing and huygens
730 data. *Icarus* 205:719–721
- 731 Lü P, Narteau C, Dong Z, Rozier O, Du Pont SC (2017) Unravelling raked
732 linear dunes to explain the coexistence of bedforms in complex dunefields.
733 *Nature communications* 8:1–9
- 734 Lü P, Narteau C, Dong Z, Claudin P, Rodriguez S, An Z, Fernandez-Cascales
735 L, Gadal C, Courrech du Pont S (2021) Direct validation of dune instability
736 theory. *Proceedings of the National Academy of Sciences* 118
- 737 Mason P, Sykes R (1979) Flow over an isolated hill of moderate slope. *Q J R
738 Meteorol Soc* 105:383–395
- 739 Mckenna Neuman C, Lancaster N, Nickling WG (1997) Relations between
740 dune morphology, air flow, and sediment flux on reversing dunes, Sil-
741 ver Peak, Nevada. *Sedimentology* 44(6):1103–1111, DOI 10.1046/j.1365-
742 3091.1997.d01-61.x
- 743 Mizumura K (1995) Free-surface profile of open-channel flow with wavy bound-
744 ary. *J Hydraul Eng* 121(7):533–539
- 745 Monin AS, Obukhov AM (1954) Basic laws of turbulent mixing in the surface
746 layer of the atmosphere. *Contrib Geophys Inst Acad Sci USSR* 151(163):e187
- 747 Mulligan KR (1988) Velocity profiles measured on the windward slope of a
748 transverse dune. *Earth Surf Process Landf* 13(7):573–582
- 749 Muñoz-Sabater J, Dutra E, Agustí-Panareda A, Albergel C, Arduini G, Bal-
750 samo G, Boussetta S, Choulga M, Harrigan S, Hersbach H, et al. (2021)
751 Era5-land: A state-of-the-art global reanalysis dataset for land applications.
752 *Earth Syst Sci Data* 13:4349–4383
- 753 Nield JM, King J, Wiggs GFS, Leyland J, Bryant RG, Chiverrell RC, Darby
754 SE, Eckhardt FD, Thomas DSG, Vircavs LH, Washington R (2014) Esti-
755 mating aerodynamic roughness over complex surface terrain. *J Geophys Res*
756 118:12948–12961
- 757 Nield JM, Wiggs GF, Baddock MC, Hipondoka MH (2017) Coupling leeside
758 rainfall to avalanche characteristics in aeolian dune dynamics. *Geology*
759 45(3):271–274
- 760 Pähzt T, Durán O (2020) Unification of aeolian and fluvial sediment transport
761 rate from granular physics. *Phys Rev Lett* 124:168001
- 762 Pearce KI, Walker IJ (2005) Frequency and magnitude biases in the 'Fryberger'
763 model, with implications for characterizing geomorphically effective winds.
764 *Geomorphology* 68:39–55
- 765 Pelletier JD, Field JP (2016) Predicting the roughness length of turbulent flows
766 over landscapes with multi-scale microtopography. *Earth Surface Dynamics*
767 4:391–405

- 768 Poggi D, Katul G, Albertson J, Ridolfi L (2007) An experimental investigation
769 of turbulent flows over a hilly surface. *Phys Fluids* 19:036601
- 770 Rasmussen KR (1989) Some aspects of flow over coastal dunes. *Proceedings of*
771 *the Royal Society of Edinburgh, Section B: Biological Sciences* 96:129–147
- 772 Rasmussen KR, Iversen JD, Rautaheimo P (1996) Saltation and wind flow
773 interaction in a variable slope wind tunnel. *Geomorphology* 17:19–28
- 774 Raupach M (1992) Drag and drag partition on rough surfaces. *Boundary-Layer*
775 *Meteorol* 60:375–395
- 776 Rubin DM, Hunter RE (1987) Bedform alignment in directionally varying
777 flows. *Science* 237:276–278
- 778 Runyon K, Bridges N, Ayoub F, Newman C, Quade J (2017) An integrated
779 model for dune morphology and sand fluxes on mars. *Earth and Planetary*
780 *Science Letters* 457:204–212
- 781 Sauermann G, Andrade Jr J, Maia L, Costa U, Araújo A, Herrmann H (2003)
782 Wind velocity and sand transport on a barchan dune. *Geomorphology* 54(3–
783 4):245–255
- 784 Seidel DJ, Zhang Y, Beljaars A, Golaz JC, Jacobson AR, Medeiros B (2012)
785 Climatology of the planetary boundary layer over the continental united
786 states and europe. *J Geophys Res* 117:D17106
- 787 Shao Y (2008) Physics and modelling of wind erosion, vol 37. Springer Science
788 & Business Media
- 789 Shen Y, Zhang C, Huang X, Wang X, Cen S (2019) The effect of wind speed
790 averaging time on sand transport estimates. *Catena* 175:286–293
- 791 Sheridan PF, Vosper SB (2006) A flow regime diagram for forecasting lee
792 waves, rotors and downslope winds. *Meteorol Appl* 13:179–195
- 793 Sherman CA (1978) A mass-consistent model for wind fields over complex
794 terrain. *J Appl Meteorol Clim* 17(3):312–319
- 795 Sherman D, Farrell E (2008) Aerodynamic roughness lengths over movable
796 beds: Comparison of wind tunnel and field data. *J Geophys Res* 113:1–10
- 797 Sherman DJ, Li B (2012) Predicting aeolian sand transport rates: A reevalu-
798 ation of models. *Aeolian Res* 3:371–378
- 799 Smith AB, Jackson DWT, Cooper JAG (2017) Three-dimensional airflow and
800 sediment transport patterns over barchan dunes. *Geomorphology* 278:28–42
- 801 Song Q, Gao X, Lei J, Li S (2019) Spatial distribution of sand dunes and their
802 relationship with fluvial systems on the southern margin of the taklimakan
803 desert, china. *Geomatics, Natural Hazards and Risk* 10:2408–2428
- 804 Spalding DB (1961) A single formula for the law of the wall. *Journal of Applied*
805 *Mechanics* 28:455–458
- 806 Stull R (2006) 9 - the atmospheric boundary layer. In: Wallace JM, Hobbs PV
807 (eds) *Atmospheric Science* (Second Edition), second edition edn, Academic
808 Press, San Diego, pp 375–417
- 809 Stull RB (1988) An introduction to boundary layer meteorology, vol 13.
810 Springer Science & Business Media
- 811 Sullivan PP, McWilliams JC (2010) Dynamics of winds and currents coupled
812 to surface waves. *Annu Rev Fluid Mech* 42:19–42

- 813 Sweet M, Kocurek G (1990) An empirical model of aeolian dune lee-face air-
814 flow. *Sedimentology* 37(6):1023–1038
- 815 Sykes RI (1980) An asymptotic theory of incompressible turbulent boundary-
816 layer flow over a small hump. *J Fluid Mech* 101:647–670
- 817 Taylor P, Teunissen H (1987) The Askervein hill project: overview and back-
818 ground data. *Boundary-Layer Meteorol* 39:15–39
- 819 Taylor P, Mason P, Bradley E (1987) Boundary-layer flow over low hills.
820 *Boundary-Layer Meteorol* 39:107–132
- 821 Tsoar H, Yaalon DH (1983) Deflection of sand movement on a sinuous longi-
822 tudinal (seif) dune: use of fluorescent dye as tracer. *Sedimentary Geology*
823 36(1):25–39
- 824 Ungar JE, Haff PK (1987) Steady state saltation in air. *Sedimentology* 34:289–
825 299
- 826 Unsworth C, Parsons D, Hardy R, Reesink A, Best J, Ashworth P, Keevil G
827 (2018) The impact of nonequilibrium flow on the structure of turbulence
828 over river dunes. *Water Resour Res* 54:6566–6584
- 829 Uppala SM, Källberg P, Simmons AJ, Andrae U, Bechtold VDC, Fiorino M,
830 Gibson J, Haseler J, Hernandez A, Kelly G, et al. (2005) The era-40 re-
831 analysis. *Q J R Meteorol Soc* 131:2961–3012
- 832 Valance A, Rasmussen K, Ould El Moctar A, Dupont P (2015) The physics
833 of aeolian sand transport. *C R Phys* 16:1–13
- 834 Venditti JG, Best JL, Church M, Hardy RJ (2013) Coherent Flow Structures
835 at Earth’s Surface. John Wiley & Sons
- 836 Virtanen P, Gommers R, Oliphant TE, Haberland M, Reddy T, Cournapeau
837 D, Burovski E, Peterson P, Weckesser W, Bright J, et al. (2020) Scipy 1.0:
838 fundamental algorithms for scientific computing in python. *Nature methods*
839 17:261–272
- 840 Vogelezang D, Holtslag A (1996) Evaluation and model impacts of alternative
841 boundary-layer height formulations. *Boundary-Layer Meteorol* 81:245–269
- 842 Vosper SB (2004) Inversion effects on mountain lee waves. *Q J R Meteorol Soc*
843 130:1723–1748
- 844 Walker I, Davidson-Arnott R, Bauer B, Hesp P, Delgado-Fernandez I, Oller-
845 head J, Smyth T (2017) Scale-dependent perspectives on the geomorphology
846 and evolution of beach-dune systems. *Earth-Science Review* 171:220–253
- 847 Walker IJ, Nickling WG (2002) Dynamics of secondary airflow and sediment
848 transport over and in the lee of transverse dunes. *Prog Phys Geogr* 26(1):47–
849 75
- 850 Walker IJ, Hesp PA, Davidson-Arnott RG, Ollerhead J (2006) Topographic
851 steering of alongshore airflow over a vegetated foredune: Greenwich dunes,
852 prince edward island, canada. *Journal of Coastal Research* 22(5):1278–1291
- 853 Walker IJ, Hesp PA, Davidson-Arnott RG, Bauer BO, Namikas SL, Ollerhead
854 J (2009) Responses of three-dimensional flow to variations in the angle of
855 incident wind and profile form of dunes: Greenwich dunes, prince edward
856 island, canada. *Geomorphology* 105:127–138
- 857 Walmsley JL, Salmon J, Taylor P (1982) On the application of a model of
858 boundary-layer flow over low hills to real terrain. *Boundary-Layer Meteorol*

- 859 23(1):17–46
- 860 Weaver C, Wiggs G (2011) Field measurements of mean and turbulent airflow
861 over a barchan sand dune. *Geomorphology* 128:32–41
- 862 Wiggs G, Bullard J, Garvey B, Castro I (2002) Interactions between airflow
863 and valley topography with implications for aeolian sediment transport.
864 *Physical Geography* 23:366–380
- 865 Wood N (2000) Wind flow over complex terrain: a historical perspective and
866 the prospect for large-eddy modelling. *Boundary-Layer Meteorol* 96(1):11–
867 32
- 868 Zhang C, Li Q, Zhou N, Zhang J, Kang L, Shen Y, Jia W (2016) Field obser-
869 vations of wind profiles and sand fluxes above the windward slope of a sand
870 dune before and after the establishment of semi-buried straw checkerboard
871 barriers. *Aeolian Res* 20:59–70
- 872 Zilker DP, Hanratty TJ (1979) Influence of the amplitude of a solid wavy wall
873 on a turbulent flow. part 2. separated flows. *J Fluid Mech* 90:257–271
- 874 Zilker DP, Cook GW, Hanratty TJ (1977) Influence of the amplitude of a solid
875 wavy wall on a turbulent flow. part 1. non-separated flows. *J Fluid Mech*
876 82:29–51

877 **Local wind regime induced by giant linear dunes**
 878 — Supplementary Material —

879 **C. Gadal* · P. Delorme · C. Narteau · G.F.S. Wiggs · M. Baddock ·**
 880 **J.M. Nield · P. Claudin**

881
 882 * Institut de Mécanique des Fluides de Toulouse, Université de Toulouse Paul
 883 Sabatier, CNRS, Toulouse INP-ENSEEIHT, Toulouse, France.
 884 cyril.gadal@imft.fr

885 **1. Shear velocity and calibration of the hydrodynamical roughness**

886 As the regionally predicted and locally measured velocities are available at
 887 different heights, we can not compare them directly. We therefore convert all
 888 velocities into shear velocities u_* , characteristic ~~of the turbulent~~ ~~the turbulent~~
 889 logarithmic velocity profile (Spalding 1961; Stull 1988):

$$\frac{u(z)}{u_*} = \frac{1}{\kappa} \ln \left(\frac{z}{z_0} \right), \quad (15)$$

890 where z is the vertical coordinate, $\kappa = 0.4$ the von Kármán constant and z_0 the
 891 hydrodynamic roughness. Note that, strickly speaking, this logarithmic profile
 892 is valid for a neutrally stratified ABL only. Vertical density gradients occuring
 893 in other conditions may thus induce large discrepancies (Monin and Obukhov 1954; Garratt 1994; Dyer 1974)
 894 . However, as our wind measurements are in the flow region close enough to
 895 the surface, where these effects are negligible, this logarithmic wind profile
 896 remains a fairly good approximation in all conditions (Gunn et al. 2021b).
 897 Several measurements of hydrodynamic roughnesses are available (Raupach
 898 1992; Bauer et al. 1992; Brown et al. 2008; Nield et al. 2014). In the absence
 899 of sediment transport, it is governed by the geometric features of the bed
 900 (Flack and Schultz 2010; Pelletier and Field 2016). When aeolian saltation
 901 occurs, it is rather controlled by the altitude of Bagnold's focal point (Durán
 902 et al. 2011; Valance et al. 2015), which depends on the wind velocity and grain
 903 properties (Sherman and Farrell 2008; Zhang et al. 2016; Field and Pelletier
 904 2018). Whether associated with geometric features or with sediment transport,
 905 its typical order of magnitude is the millimetre scale on sandy surfaces.

906 We do not have precise velocity vertical profiles to be able to deduce an
 907 accurate value of z_0 in the various environments of the meteorological stations
 908 (vegetated, arid, sandy). Our approach is to rather select the hydrodynamic
 909 roughness which allows for the best possible matching between the regionally
 910 predicted and locally measured winds, i.e. minimising the relative difference δ
 911 between the wind vectors of both datasets:

$$\delta = \frac{\sqrt{\langle \| \mathbf{u}_{*,\text{era}} - \mathbf{u}_{*,\text{station}} \|^2 \rangle}}{\sqrt{\langle \| \mathbf{u}_{*,\text{era}} \|^2 \rangle \langle \| \mathbf{u}_{*,\text{station}} \|^2 \rangle}}, \quad (16)$$

where $\langle \cdot \rangle$ denotes time average. This parameter is computed for values of z_0 in ERA5-Land analysis ranging from 10^{-5} m to 10^{-2} m for the four different stations. Note that for the North Sand Sea and South Sand Sea stations, where the giant dunes feedback presumably affect the wind, we take into account the non-deflected winds only in the calculation of δ (with a 15° tolerance).

As shown in Online Resource Fig. S4S3, the minimum values of δ in the space $(z_0^{\text{ERA5Land}}, z_0^{\text{local}})$ form a line. We thus set the roughness in the ERA5-Land analysis to the typical value $z_0 = 10^{-3}$ m, and deduce the corresponding ones for the local stations. It leads to 2.7, 0.8, 0.1 and 0.5 mm for the Etosha West, North Sand Sea, Huab and South Sand Sea stations, respectively. Importantly, this approach somewhat impacts the calculation of the shear velocities, but not that of the wind directions. As such, most of our conclusions are independent of such a choice. However, it may affect the magnitude of the wind velocity attenuation/amplification in flow confinement situations.

2. Computation of the ABL characteristics

The estimation of the non-dimensional numbers associated with the ABL requires the computation of representative meteorological quantities. In arid areas, the vertical structure of the atmosphere can be approximated by a well mixed convective boundary layer of height H , topped by the stratified free atmosphere (Stull 1988; Shao 2008). In this context, one usually introduces the virtual potential temperature T_{vp} , which is a constant T_0 inside the boundary layer, and increases linearly in the FA (Online Resource Fig. S12S8a):

$$T_{\text{vp}}(z) = \begin{cases} T_0 & \text{for } z \leq H, \\ T_0 \left(1 + \frac{\Delta T_{\text{vp}}}{T_0} + \frac{N^2}{g}(z - H) \right) & \text{for } z \geq H, \end{cases} \quad (17)$$

where ΔT_{vp} is the temperature discontinuity at the capping layer and $N = \sqrt{g \partial_z T_{\text{vp}} / T_0}$ is the Brunt-Väisälä frequency, characteristic of the stratification. Note that, under the usual Boussinesq approximation, temperature and air density variations are simply related by $\delta T_{\text{vp}}/T_0 \simeq -\delta\rho/\rho_0$ (see Online Resource of Andreotti et al. (2009)), so that N can equivalently be defined from the density gradient as next to Eq. 4(1).

The ERA5 dataset provides vertical profiles of the geopotential ϕ , the actual temperature T and the specific humidity η at given pressure levels P . The vertical coordinate is then calculated as:

$$z = \frac{\phi R_t}{g R_t - \phi}, \quad (18)$$

where $R_t = 6371229$ m is the reference Earth radius and $g = 9.81$ m s $^{-2}$ is the gravitational acceleration. One also computes the virtual potential temperature as:

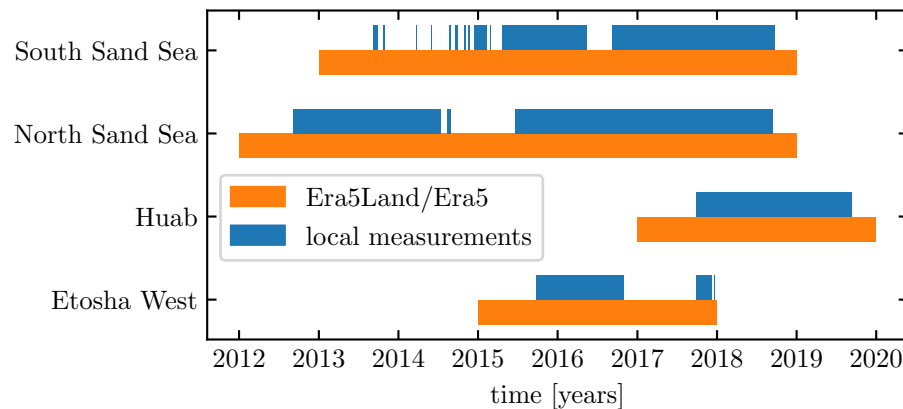
$$T_{\text{vp}} = T \left[1 + \left(\frac{M_d}{M_w} - 1 \right) \eta \right] \left(\frac{P_0}{P} \right)^{R/C_p}, \quad (19)$$

where $P_0 = 10^5$ Pa is the standard pressure, $R = 8.31$ J/K is the ideal gas constant, $C_p \simeq 29.1$ J/K is the air molar heat capacity, and $M_w = 0.018$ kg/Mol and $M_d = 0.029$ kg/Mol are the molecular masses of water and dry air respectively. The specific humidity is related to the vapour pressure p_w as

$$\eta = \frac{\frac{M_w}{M_d} p_w}{p - \left(1 - \frac{M_w}{M_d}\right) p_w}. \quad (20)$$

The ERA5 dataset also provides an estimate of the ABL depth H , based on the behaviour of the Richardson vertical profile. This dimensionless number is defined as the ratio of buoyancy and flow shear terms, and can be expressed as $\text{Ri} = N^2 / (\partial_z u)^2$. It vanishes in the lower well-mixed layer where T_{vp} is constant, and increases in the stratified FA. Following the method and calibration of Vogelegang and Holtlag (1996); Seidel et al. (2012), the value $\text{Ri}(z) \simeq 0.25$ has been shown to be a good empirical criterion to give $z \simeq H$ within a precision varying from 50% for the shallower ABL (e.g. at night) to 20% for situations of stronger convection.

Examples of vertical profiles of the virtual potential temperature deduced from ERA5 are shown in Online Resource Fig. S12S8a. For each of them, an average temperature is computed below the ABL depth ($z < H$), and a linear function is fitted above, allowing us to extract the temperature jump ΔT_{vp} . Importantly, some profiles display a vertical structure that cannot be approximated by the simple form (17) used here (Online Resource Fig. S12S8b). In practice, we removed from the analysis all of those leading to the unphysical case $\Delta T_{\text{vp}} < 0$. We have noticed that these ‘ill-processed’ profiles dominantly occur in winter and are evenly spread across the hours of the day. Importantly, they represent $\simeq 12\%$ of the data only (Online Resource Fig. S12S8c,d), and we are thus confident that this data treatment does not affect our conclusions.



Gant chart representing the valid time steps for the two data sets, for all stations.

Fig. S1 ~~Photographs of the meteorological stations. a: South Sand Sea station. b–e: North Sand Sea station. d: Huab station. e: Etosha West station.~~

Gant chart representing the valid time steps for the two data sets, for all stations.

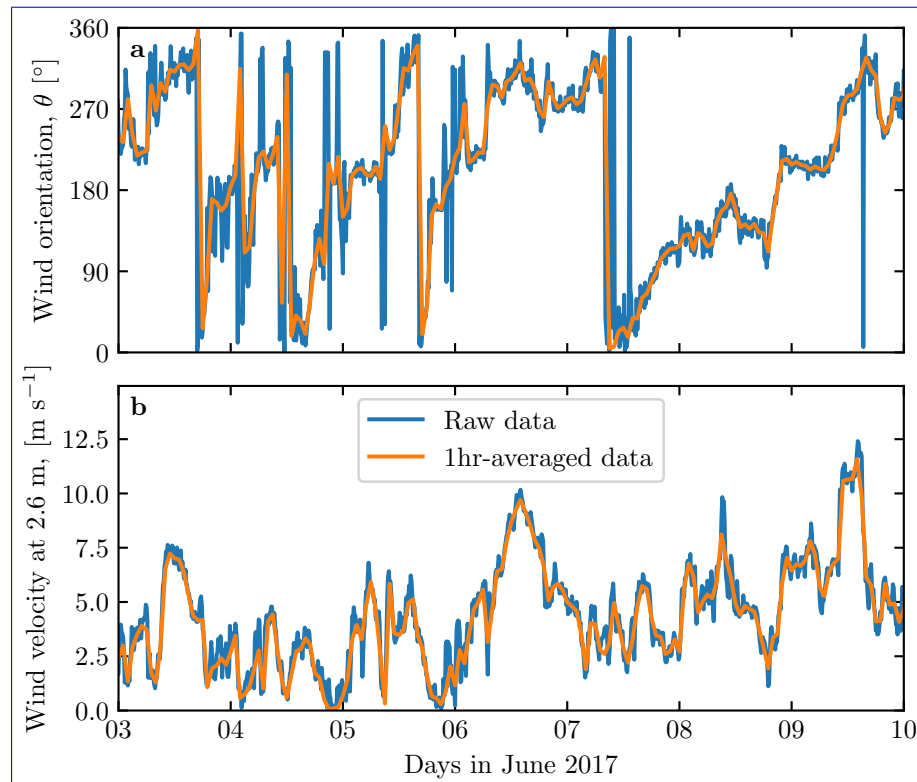


Fig. S2 Comparison between raw local wind measurements, and hourly-averaged data for South Sand Sea station. **a:** wind direction. **b:** wind velocity at height 2.6 m.

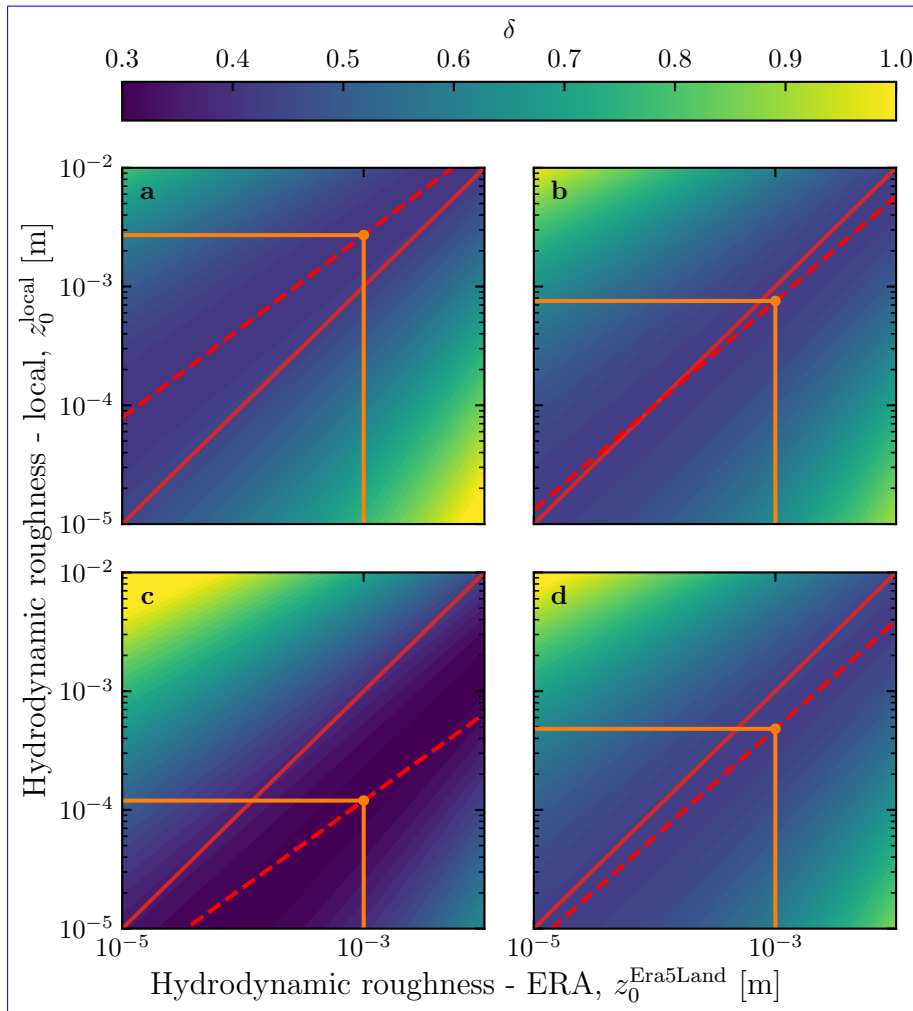


Fig. S3 Calibration of hydrodynamic roughness. The parameter δ (Eq. 16) quantifying the difference between local and predicted winds is shown in colorscale as a function of the hydrodynamic roughnesses chosen for the ERA5-Land and for local winds, for the (a) Etosha West, (b) North Sand Sea, (c) Huab and (d) South Sand Sea stations. The red dashed and plain lines shows the minima of δ and the identity line, respectively. The orange lines and dots highlight the chosen hydrodynamic roughnesses for the local winds deduced from setting $z_0^{\text{ERA5Land}} = 1 \text{ mm}$.

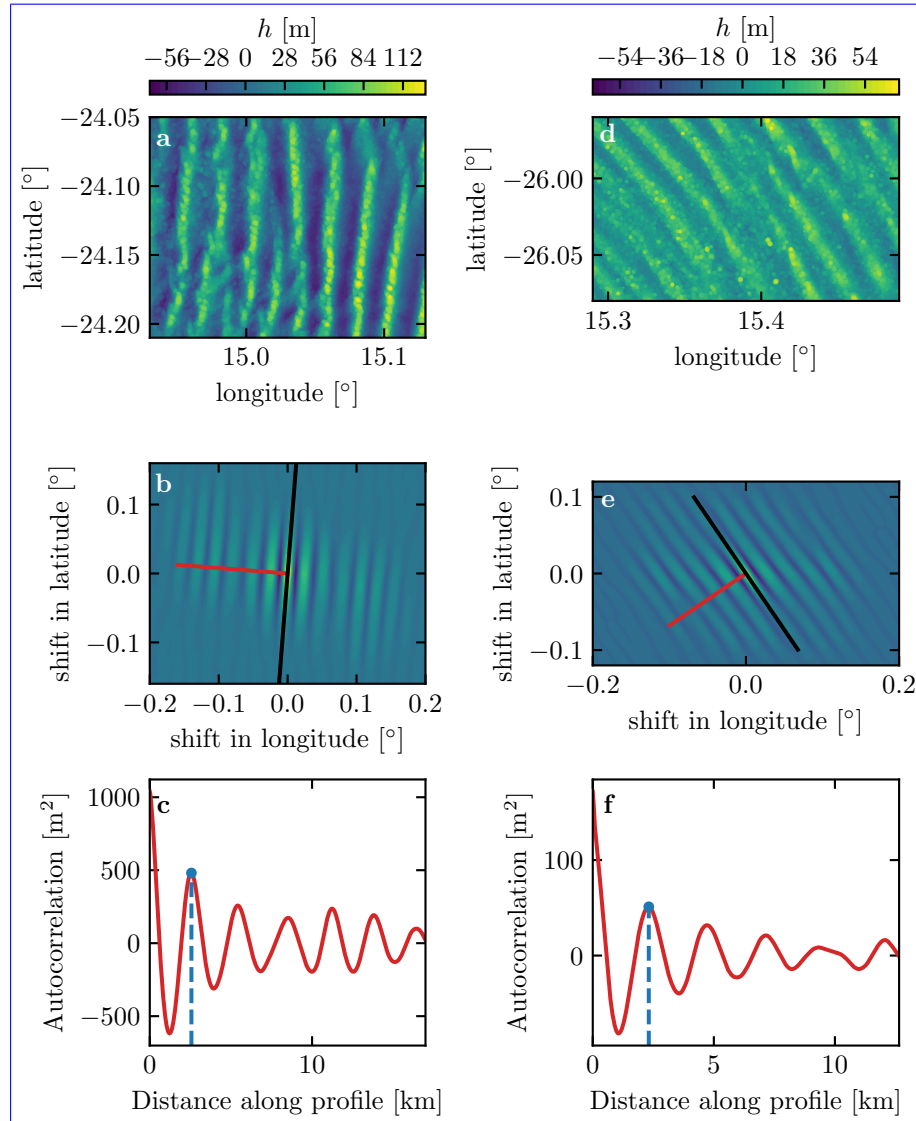


Fig. S4 Analysis of the DEMs of the North Sand Sea (left column – panels a, b, c) and South Sand Sea (right column – panels d, e, f) stations. **a–d:** Bed elevation detrended by a fitted second order polynomial base-line. **b–e:** Autocorrelation matrix shown in colorscale. The black line shows the detected dune orientation, and the red line represents the autocorrelation profile along which the dune wavelength is calculated, displayed in **c–f**. The blue lines and dots show the first peak of the autocorrelation profile, whose abscissa gives the characteristic wavelength of the dune pattern.

Temporal comparison between the wind data coming from the ERA5-Land climate reanalysis (orange lines) and from the local measurements (blue lines). Coloured swathes indicate day (between 1000 UTC and 2200 UTC) and night (before 1000 UTC or after 2200 UTC). **a–b:** Huab station in summer. **b–c:** Huab station in winter. **d–e:** South Sand Sea station in summer. **f–g:** South Sand Sea station in winter.

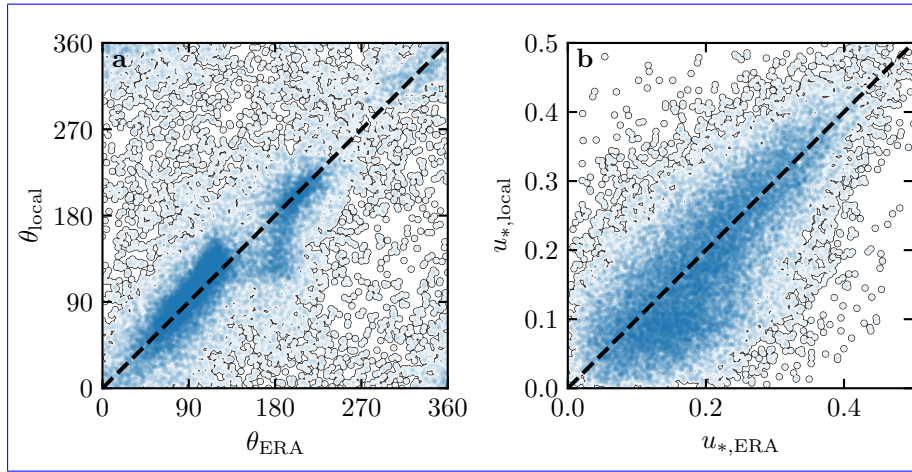


Fig. S5 Statistical comparison of the wind orientation (a) and velocity (b) between the ERA5-Land dataset and the local measurements for the Huab and Etosha West stations. Data point clustering around identity lines (dashed and black) provide evidence for agreement of the two sets.

Distributions of wind direction at the South Sand Sea Station for the ERA5-Land climate reanalysis (orange) and the local measurements (blue)—equivalent of Fig. 3. In each subplot, both distributions are plotted from the same time steps, selected with constraints on the wind direction (columns) and/or wind velocity (rows) in the ERA5-Land dataset. The gray vertical dashed lines indicate the dune orientation. The numbers at the top centre give the percentage of time steps selected in each sub-range, as well as the percentage of them corresponding to the day (between 1000 UTC and 2200 UTC). The purple frame highlights the regime (small wind velocities, nocturnal summer wind) during which the wind data from both datasets differ.

Distributions of wind direction at the Huab and Etosha West stations for the ERA5-Land climate reanalysis (orange) and the local measurements (blue). In each subplot, both distributions are plotted from the same time steps, selected with constraints on the wind velocity (rows) in the ERA5-Land dataset. The numbers at the top centre give the percentage of time steps selected in each sub-range, as well as the percentage of them corresponding to the day (between 1000 UTC and 2200 UTC). Compared to the North and South Namib stations (Fig. 3 and Fig. S8), histograms match for high and low velocities.

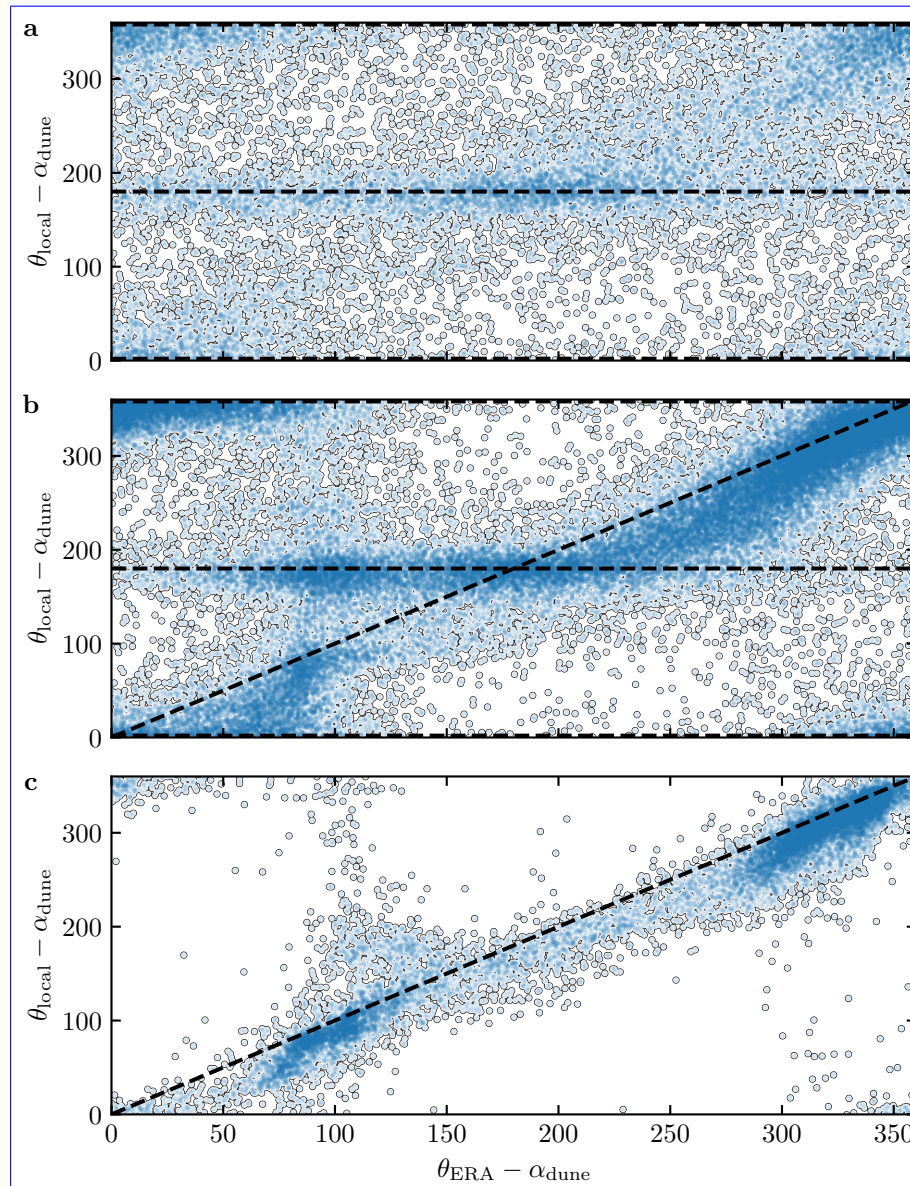


Fig. S6 Statistical comparison of the wind orientation between the ERA5-Land dataset and the local measurements for the South Sand Sea and North Sand Sea stations, for different velocity ranges. **a:** $u_{*,\text{ERA}} < 0.1 \text{ m s}^{-1}$. **b:** $0.1 < u_{*,\text{ERA}} \leq 0.25 \text{ m s}^{-1}$. **c:** $u_{*,\text{ERA}} \geq 0.25 \text{ m s}^{-1}$. The measured dune orientations are subtracted to the wind orientation, which allows us to plot both stations on the same graph. Black dashed lines indicate locally measured orientations aligned with the dune crests (here 0° , 180° and 360° – panels **a, b**), as well as the identity lines (panels **b, c**).

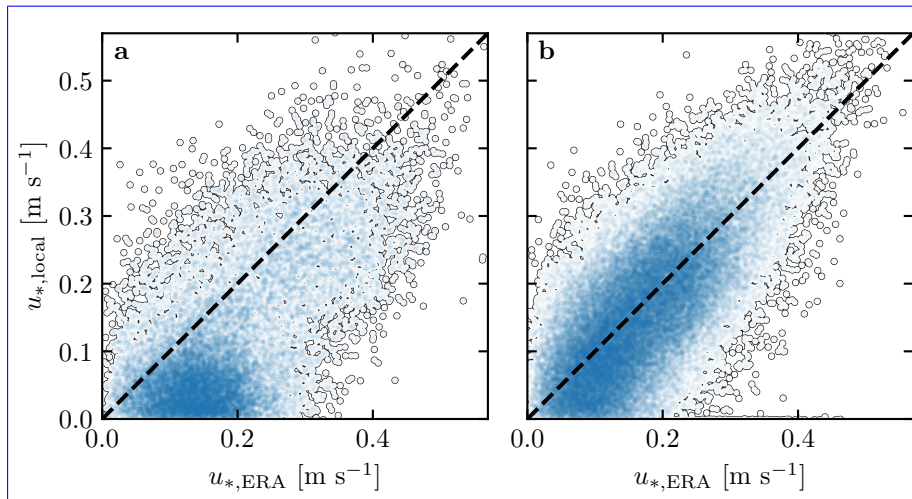


Fig. S7 Statistical comparison of the wind velocity between the ERA5-Land dataset and the local measurements for the South Sand Sea and North Sand Sea stations. **a:** Nocturnal summer easterly wind. **b:** Diurnal southerly wind. Black dashed lines are identity lines. The angle ranges used to select diurnal and nocturnal summer winds are the same as those in [FigFigs. 3–4](#) and [Online Resourcee FigFigs. S86 of the main article](#).

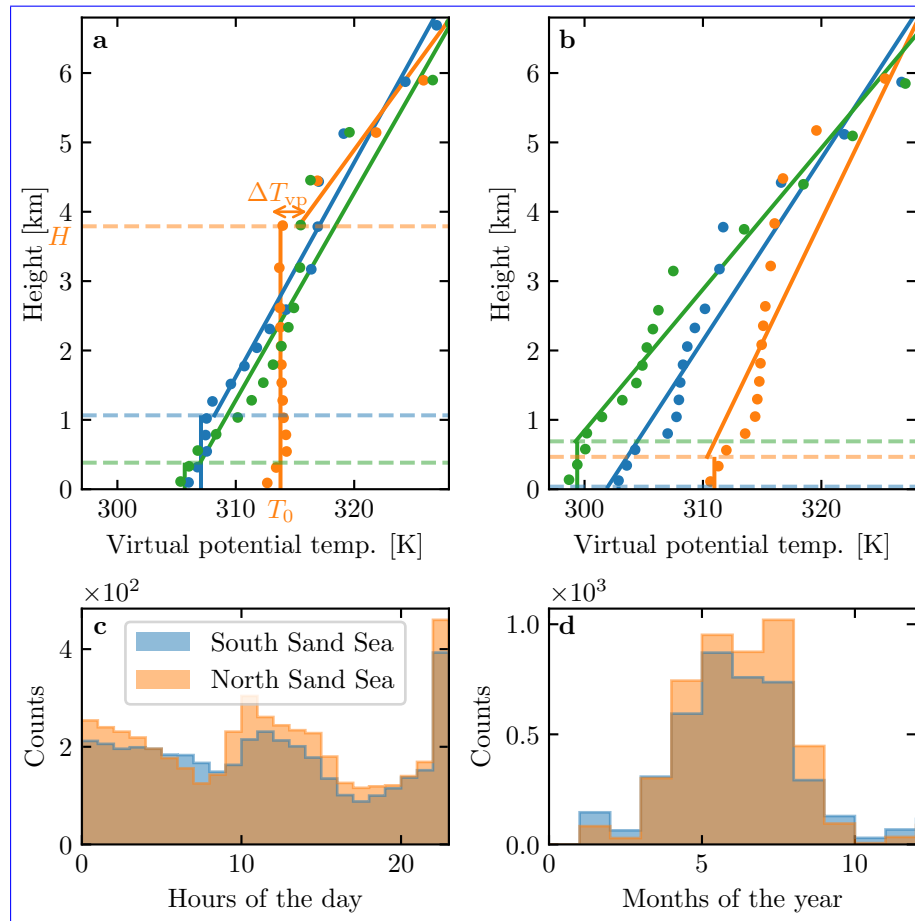


Fig. S8 **a:** Vertical profiles of the virtual potential temperature at three different times (blue: 29/11/2012 - 1100 UTC, orange: 21/03/2017 - 1200 UTC, green: 21/03/2017 - 2000 UTC) at the South Sand Sea station. Dots: data from the ERA5 reanalysis. Dashed lines: boundary layer height given by the ERA5 reanalysis. Plain lines: vertical (ABL) and linear (FA) fits to estimate the quantities displayed in Online Resource Fig. S13S9. **b:** Examples of ill-processed vertical profiles at three different times (blue: 2/12/2013 - 2300 UTC, orange: 20/03/2017 - 0000 UTC, green: 14/07/2017 - 1400 UTC) at the South Sand Sea station. **c:** Hourly distribution of ill-processed vertical profiles. **d:** Monthly distribution of ill-processed vertical profiles.

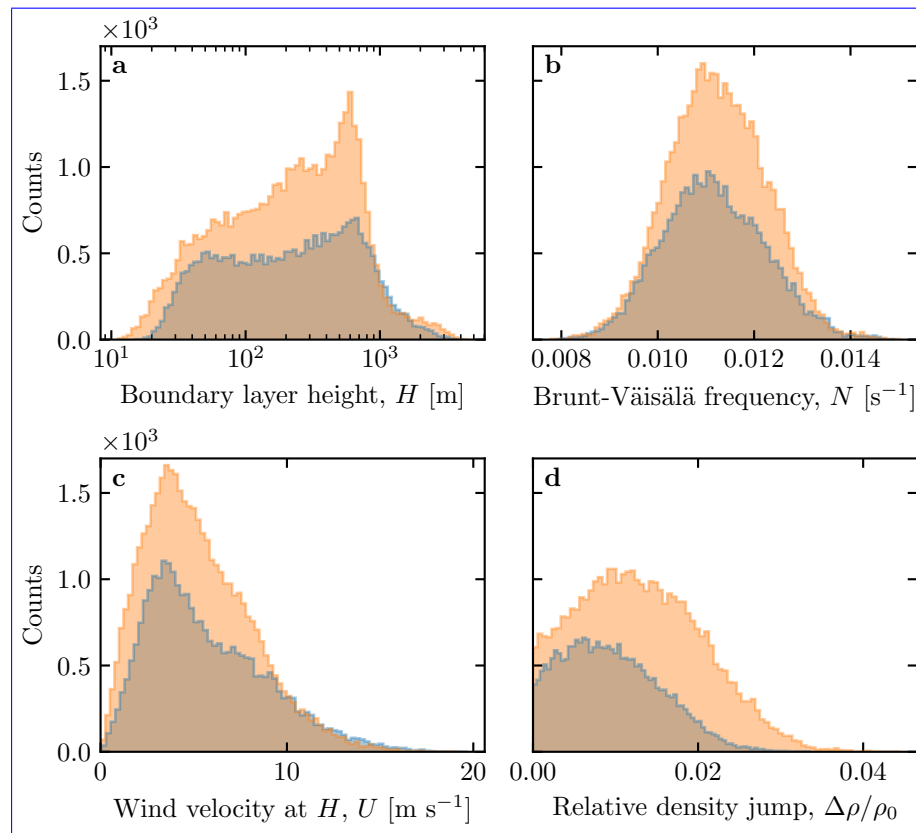


Fig. S9 Distributions of the meteorological parameters resulting from the processing of the ERA5-Land data for the South Sand Sea (blue) and the North Sand Sea (orange) stations.

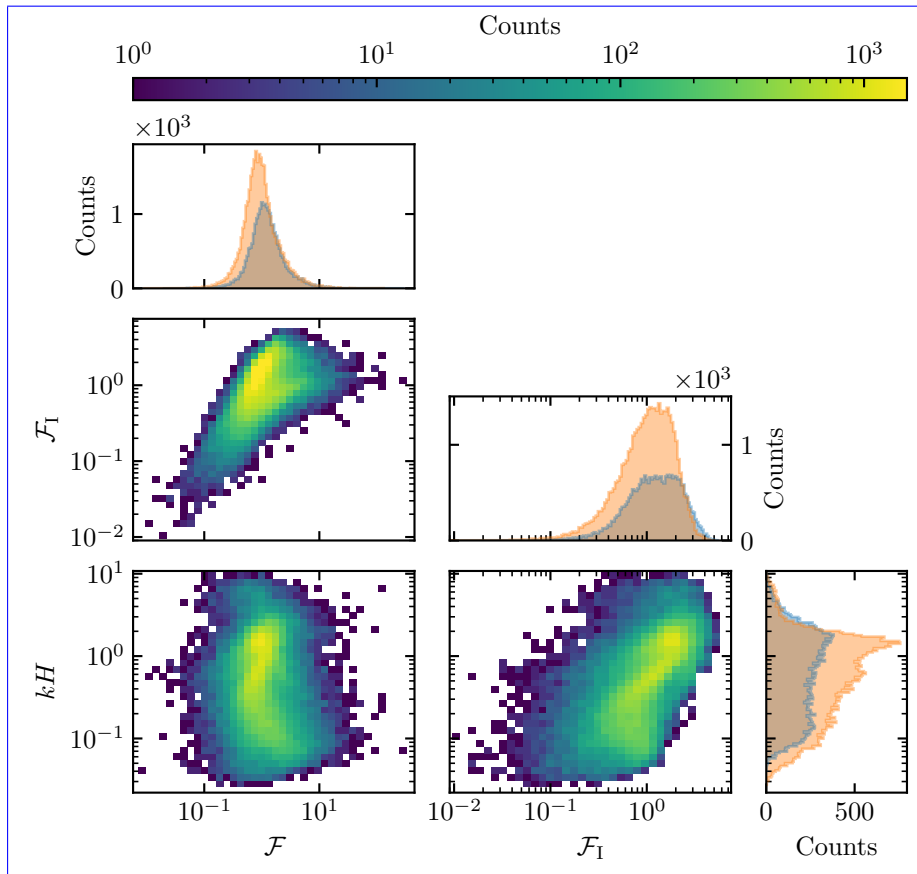


Fig. S10 Non-dimensional parameters distributions. For the marginal distributions, the orange correspond to the South Sand Sea station, and the blue to the North Sand Sea station.

Regime diagrams of the wind deviation δ_θ and relative attenuation/amplification δ_u in the spaces (\mathcal{F}_I, kH) and $(\mathcal{F}_I, \mathcal{F})$, containing the data from both the North Sand Sea and South Sand Sea stations. Green dashed lines empirically delimit the different regimes. The point density in each bin of the diagrams is shown in Online Resource Fig. S14 – 95% of the data occur in the range $-1 < \delta u < 1$. The similar regime diagrams in the space (\mathcal{F}, kH) are shown in Fig. 5.

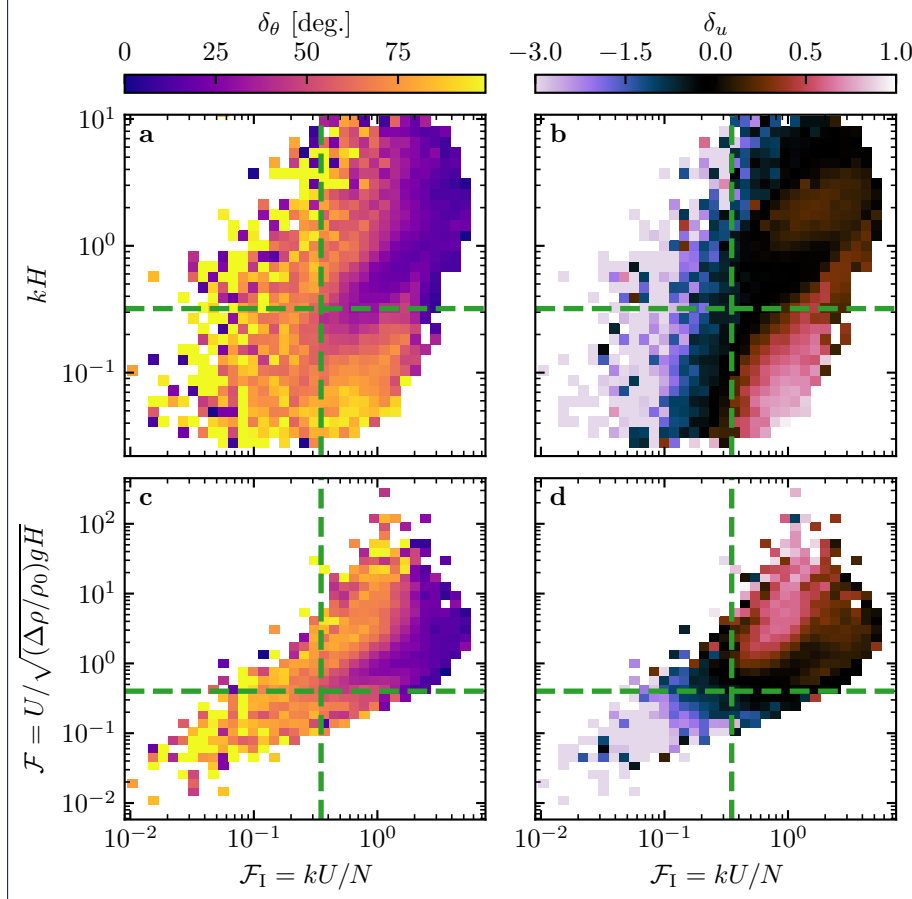


Fig. S11 Regime diagrams of the wind deviation δ_θ and relative attenuation/amplification δ_u in the spaces (\mathcal{F}_I, kH) and $(\mathcal{F}_I, \mathcal{F})$, containing the data from both the North Sand Sea and South Sand Sea stations. Green dashed lines empirically delimit the different regimes. The point density in each bin of the diagrams is shown in Online Resource Fig. S10 – 95% of the data occur in the range $-1 < \delta u < 1$. The similar regime diagrams in the space (\mathcal{F}, kH) are shown in Fig. 8.

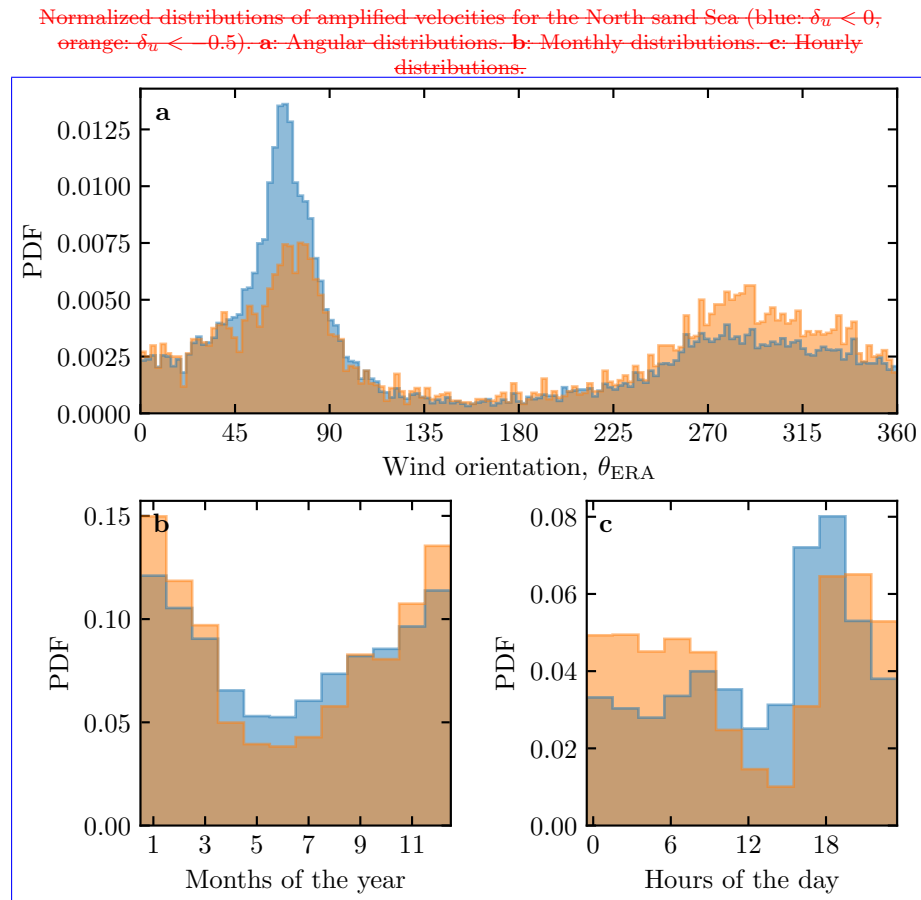


Fig. S12 Normalized distributions of amplified velocities for the North sand Sea (blue: $\delta_u < 0$, orange: $\delta_u > -0.5$). **a:** Angular distributions. **b:** Monthly distributions. **c:** Hourly distributions.

Computation of the flow disturbance with the linear model of Andreotti et al. (2009). **a** and **b** Magnitude of the hydrodynamic coefficients A_0 and B_0 , calculated from the values of the non-dimensional numbers corresponding to the ERA5 Land time series presented in Figs. 4 and 5. **c** Shear velocity streamlines over sinusoidal ridges of amplitude $k\xi_0 = 0.1$ and for increasing values of $\sqrt{A_0^2 + B_0^2}$. From the upper to the lower streamline, values of $(kH, \mathcal{F}, \mathcal{F}_I, A_0, B_0, \sqrt{A_0^2 + B_0^2})$ are (1.9, 0.6, 1.5, 3.4, 1.0, 3.5), (1.5, 0.3, 0.4, 4.8, 1.4, 5.0), (0.1, 3.5, 1.0, 8.6, 0.1, 8.6), (0.5, 0.05, 0.04, 9.6, 2.5, 9.9).

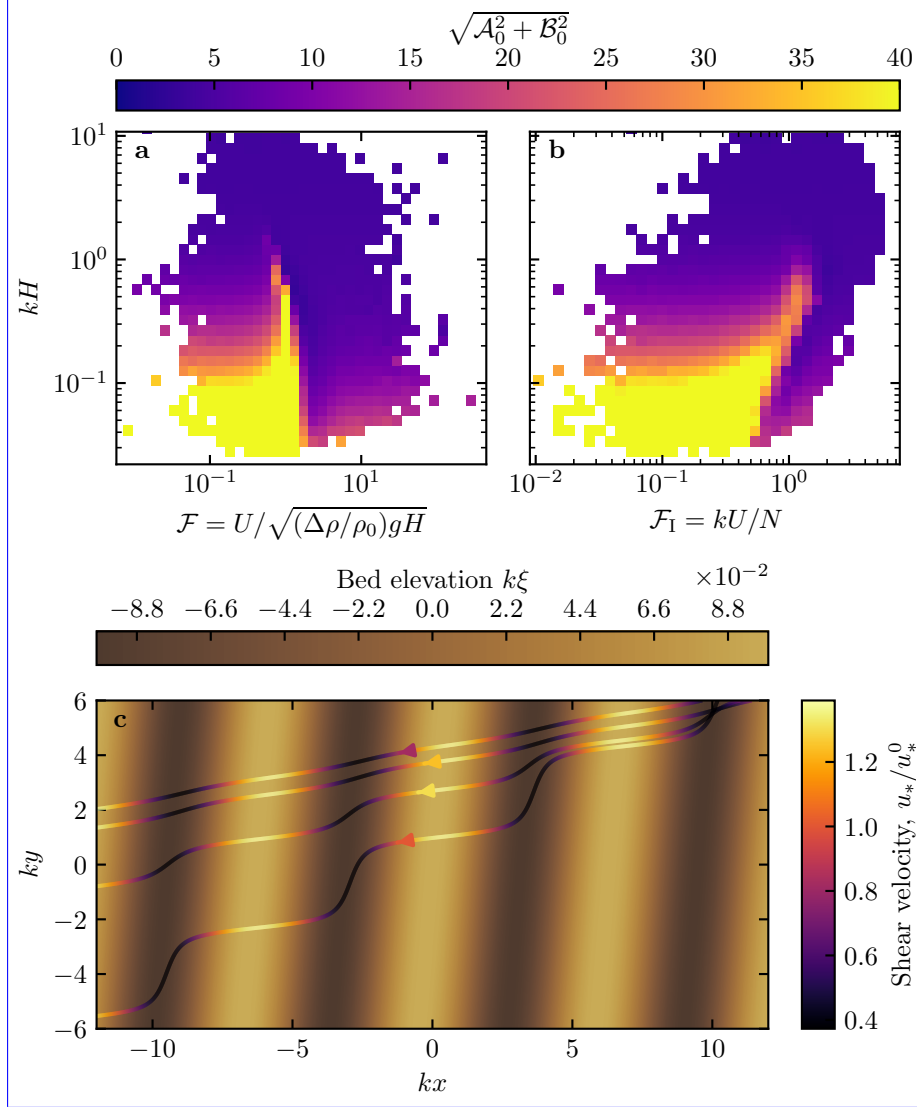


Fig. S13 Computation of the flow disturbance with the linear model of Andreotti et al. (2009). **a–b:** Magnitude of the hydrodynamic coefficients A_0 and B_0 , calculated from the time series of the non-dimensional numbers corresponding to the ERA5-Land wind data and ERA5 data on vertical pressure levels. **c:** Shear velocity streamlines over sinusoidal ridges of amplitude $k\xi_0 = 0.1$ and for increasing values of $\sqrt{A_0^2 + B_0^2}$. From the upper to the lower streamline, values of $(kH, \mathcal{F}, \mathcal{F}_I, A_0, B_0, \sqrt{A_0^2 + B_0^2})$ are (1.9, 0.6, 1.5, 3.4, 1.0, 3.5), (1.5, 0.3, 0.4, 4.8, 1.4, 5.0), (0.1, 3.5, 1.0, 8.6, 0.1, 8.6), (0.5, 0.05, 0.04, 9.6, 2.5, 9.9).

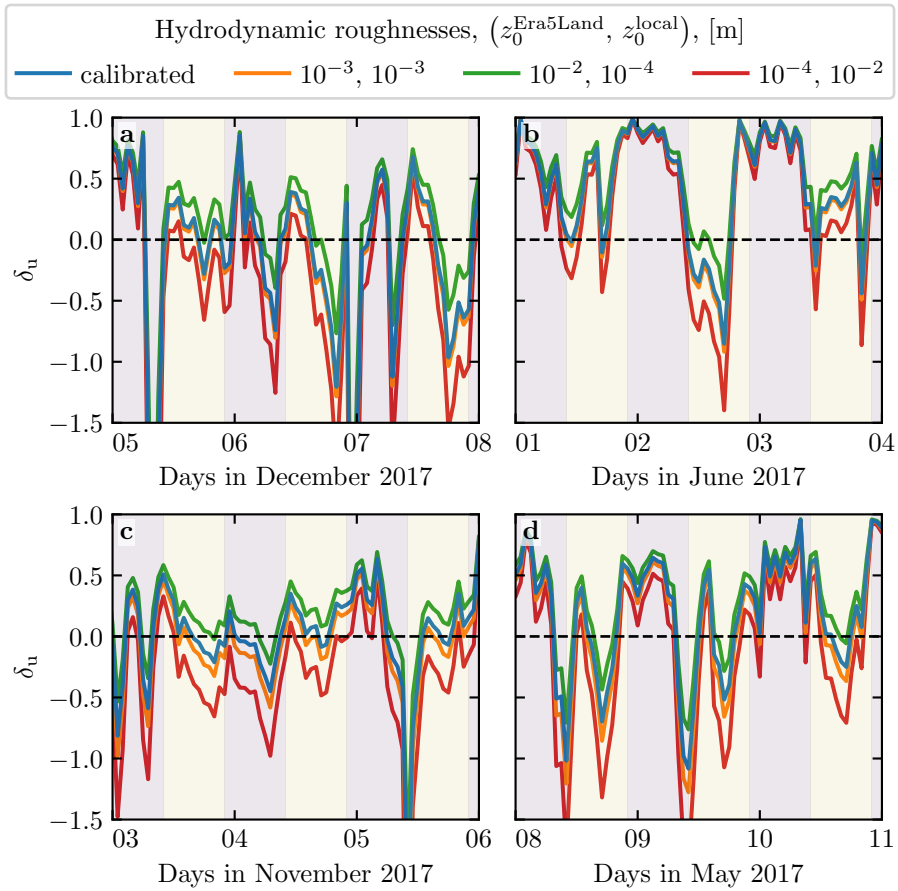


Fig. S14 Time series of the relative velocity disturbance δ_u corresponding to Fig. 5, for different values of the hydrodynamic roughnesses. **a:** North Sand Sea – summer. **b:** North Sand Sea – winter. **c:** South Sand Sea – summer. **d:** South Sand Sea – winter. Note that δ_θ is independent of the choice of z_0^{Era5Land} and z_0^{local} .